

# Floods and Heavy Precipitation at the Global Scale: 100-year Analysis and 180-year Reconstruction

B. Renard<sup>1,2,3</sup>, D. McInerney<sup>2</sup>, S. Westra<sup>2</sup>, M. Leonard<sup>2</sup>, D. Kavetski<sup>2</sup>, M.  
Thyer<sup>2</sup>, J.-P. Vidal<sup>1</sup>

<sup>1</sup>INRAE, RiverLy, Lyon, France

<sup>2</sup>School of Civil, Environmental and Mining Engineering, University of Adelaide, Adelaide, South  
Australia, Australia

<sup>3</sup>INRAE, Aix Marseille Univ, RECOVER, Aix-En-Provence, France

## Key Points:

- We perform a joint analysis of station-based flood and heavy precipitation data, at the global scale and over a long 100-year period
- Results highlight wide-ranging increasing trends affecting heavy precipitation, whereas flood trends appear weaker and less consistent
- A 180-year reconstruction of flood and heavy precipitation probabilities is proposed, using atmospheric predictors from the 20CR reanalysis

16 **Abstract**

17 Floods and heavy precipitation have disruptive impacts worldwide, but their his-  
 18 torical variability remains only partially understood at the global scale. This article aims  
 19 at reducing this knowledge gap by jointly analyzing seasonal maxima of streamflow and  
 20 precipitation at more than 3,000 stations over a 100-year period.

21 The analysis is based on Hidden Climate Indices (HCIs). Like standard climate in-  
 22 dices (e.g. Nino 3.4, NAO), HCIs are used as covariates explaining the temporal vari-  
 23 ability of data, but unlike them, HCIs are estimated from the data. In this work, a dis-  
 24 tinction is made between common HCIs, that affect both heavy precipitation and floods,  
 25 and specific HCIs, that exclusively affect one or the other. Overall, HCIs do not show  
 26 noticeable autocorrelation, but some are affected by noticeable trends. In particular, strong  
 27 and wide-ranging trends are identified in precipitation-specific HCIs, while trends affect-  
 28 ing flood-specific HCIs are weaker and have more localized effects.

29 A probabilistic model is then derived to link HCIs and large-scale atmospheric vari-  
 30 ables (pressure, wind, temperature) and to reconstruct HCIs since 1836 using the 20CRv3  
 31 reanalysis. In turn this allows estimating the probability of occurrence of floods and heavy  
 32 precipitation at the global scale. This 180-year reconstruction highlights flood hot-spots  
 33 and hot-moments in the distant past, well before the establishment of perennial mon-  
 34 itoring networks. The approach presented in this study is generic and paves the way for  
 35 an improved characterization of historical variability by making a better use of long but  
 36 highly irregular station datasets.

37 **Plain Language Summary**

38 Floods and heavy precipitation events still hold some mystery despite their disrup-  
 39 tive impacts. As an illustration, the latest IPCC report (recently released in 2021) in-  
 40 dicates that "the frequency and intensity of heavy precipitation events have increased  
 41 since the 1950s", but that at the same time "confidence about peak flow trends over past  
 42 decades on the global scale is low". Why this apparent disconnect between floods and  
 43 heavy precipitation? Beyond trends, do floods and heavy precipitation vary together at  
 44 the global scale? How are they related to atmospheric variables such as winds, temper-  
 45 ature, atmospheric pressure?

46 This article describes a 100-year analysis of floods and heavy precipitation data at  
47 the global scale. This analysis is made possible by an original probabilistic model adapted  
48 to station datasets with highly variable data availability (<https://vimeo.com/802751683>).  
49 The analysis first highlights wide-ranging increasing trends affecting heavy precipitation,  
50 whereas flood trends appeared weaker and less consistent. It is then used to identify cli-  
51 mate configurations associated with the occurrence of floods and heavy precipitation,  
52 and to build a 180-year (1836-2015) reconstruction of floods and heavy precipitation prob-  
53 abilities at the global scale. This contributes to a better understanding of the histori-  
54 cal variability of hydrologic extremes in the distant past.

## 55 1 Introduction

56 Understanding the historical variability of floods and heavy precipitation in the con-  
57 text of a changing climate is an important endeavor (Sharma et al., 2018). At a global  
58 scale, this understanding is hampered by the spatial sparsity of station data and the scarcity  
59 of long series spanning more than 50 years. Yet some long series do exist and may be  
60 highly informative when analyzed with adapted methods. The first aim of this work is  
61 hence to provide a 100-year global analysis of the joint historical variability of floods and  
62 heavy precipitation, and to compare the outcome with literature results mostly based  
63 on shorter 50-to-60-year analysis periods. The second aim is to infer relations between  
64 hydrologic extremes and large-scale climate variables from this long analysis, and to use  
65 these relations to estimate probabilities of occurrence of extremes since 1836 at the global  
66 scale.

67 Many studies have analyzed historical changes in floods and heavy precipitation,  
68 as summarized in the latest IPCC report (IPCC, 2021, chapters 8 and 11). Focusing on  
69 large-scale studies, there is now growing evidence that heavy precipitation has increased  
70 over land since the 1950's (e.g. Westra et al., 2012; Papalexiou & Montanari, 2019; Dunn  
71 et al., 2020; Q. Sun et al., 2021). This overall increase is consistent with the larger water-  
72 holding capacity of a warmer atmosphere, but regional differences indicate that dynamic  
73 changes (e.g. change in storms trajectory) may play a role as well. In contrast, flood changes  
74 do not show such a consistent signal. Continental-scale studies generally find a mixture  
75 of increasing and decreasing trends, with many regions showing no discernible signal at  
76 all (e.g. Berghuijs et al., 2017; Hodgkins et al., 2017; Do et al., 2017; Blöschl, Hall, et  
77 al., 2019; Gudmundsson et al., 2019; L. Slater et al., 2021). While the discrepancy be-

tween the consistent signal found for precipitation and the lack thereof for floods may appear surprising at first sight, it can be explained by the diversity and the complexity of flood-generating mechanisms (Sharma et al., 2018). For instance, Tramblay et al. (2019) showed that antecedent moisture conditions could resolve an apparent contradiction between increasing heavy precipitation and decreasing floods in Mediterranean France. Brunner et al. (2021) also demonstrated the existence of a catchment-specific threshold below which flood changes do not reflect precipitation changes due to the confounding effect of land surface processes. Alternatively, one of the few robust flood signals is the change in flood timing for snowmelt regimes (e.g. Blöschl et al., 2017; Burn & Whitfield, 2017; Dudley et al., 2017), which is temperature-driven rather than precipitation-driven.

Although trends have been the focus of a majority of papers studying the historical variability of floods and heavy precipitation, other forms of temporal variability have also been studied. For instance, the tendency of events to cluster into flood-rich and flood-poor periods has attracted attention (Hall et al., 2014; Blöschl, Bierkens, et al., 2019) and has been highlighted in some regions of Australia (Franks & Kuczera, 2002; Liu & Zhang, 2017) or Europe (Merz et al., 2016; Lun et al., 2020). Such a low frequency variability, also referred to as persistence, may result from the influence of oceanic modes of climate variability such as the Pacific Decadal Oscillation (Wei et al., 2021).

Detecting trends, persistence or any other type of temporal variability using station data faces several methodological challenges, as reviewed by L. J. Slater et al. (2020). The most typical approach used in the literature is to analyze each site separately, and then to look for coherent patterns using, for example, mapping or kriging of at-site results. This is the simplest approach but the limited length of many station series may induce a large sampling uncertainty and hence limits the power to detect trends or the ability to model more complex temporal structures (Bertola et al., 2020). The analysis is also generally restricted to a common period for all sites in order to make at-site results comparable, hence discarding valuable older data.

An alternative approach is to aggregate local series at the level of predefined regions, typically using spatial averaging (e.g. Papalexiou & Montanari, 2019) or by counting events (e.g. Hodgkins et al., 2017; Najibi & Devineni, 2018). The rationale behind this aggregation is to reduce the variability of local series in order to increase statistical power. However this approach still requires working with a short common period to

110 avoid inhomogeneities due to a varying number of aggregated sites. Limitations for de-  
111 tecting a low-frequency signal using short series hence remain. The regions also need to  
112 be defined carefully since opposite trends within a region may cancel out.

113 A third approach is based on spatial modeling. The principle is to use the origi-  
114 nal at-site series within a probabilistic model that makes explicit assumptions on how  
115 trends or other variability components vary across stations (e.g. Renard et al., 2006, 2008;  
116 Aryal et al., 2009; X. Sun & Lall, 2015; Bertola et al., 2020, 2021). This reduces esti-  
117 mation uncertainties at the cost of making assumptions that need scrutiny. It is also more  
118 complex to implement than the previous approaches because it requires accounting for  
119 spatial dependence and missing data, and it typically leads to a high-dimensional infer-  
120 ence problem.

121 Beyond these methodological challenges, analyzing the historical variability of floods  
122 and heavy precipitation also faces the difficulty of handling station datasets with highly  
123 irregular data availability. It is striking to observe that most contributions to the lat-  
124 est IPCC report use analysis periods starting around 1960 and rarely before 1950 (IPCC,  
125 2021, see also a few examples in Table 1). There exist a few exceptions using  $\sim$ 100-year  
126 long periods (e.g. Mediero et al., 2015; Burn & Whitfield, 2018; Q. Sun et al., 2021) but  
127 with a drastically reduced number of stations. In other words, most studies restrict them-  
128 selves to short periods common to many sites or long periods common to a few sites, whereas  
129 station datasets often increase in data availability as the measurement network grows  
130 (see Figure 1 for an illustration). As discussed in previous paragraphs, this restriction  
131 often results from methodological constraints and is hence not unavoidable. For instance,  
132 the Hidden Climate Indices (HCI) approach proposed by Renard et al. (2021) accom-  
133 modates such growing datasets, and leads to estimates related to sparsely represented  
134 regions or periods being affected by larger uncertainties.

135 Another approach to alleviate the limitations of short and irregular datasets is to  
136 build reconstructed series, generally by downscaling long reanalyses such as 20CR (Compo  
137 et al., 2011). In France for instance, daily precipitation and temperature series have been  
138 reconstructed since 1871 (Radanovics et al., 2013; Caillouet et al., 2016; Devers et al.,  
139 2020, 2021), and have been transformed into catchment-scale streamflow series by hy-  
140 drologic modeling (Caillouet et al., 2017; Bonnet et al., 2017; Caillouet et al., 2021). At  
141 a larger continental or global scale, a related approach uses the outputs of global hydro-

142 logic models (Stahl et al., 2012). However, the existence of large inconsistencies between  
143 observed and modeled flood trends (Do et al., 2020) casts doubt on the adequacy of global  
144 hydrologic models to represent extremes in small to moderately-sized catchments. The  
145 latter generally constitute the majority of catchments monitored in station datasets and  
146 may also represent major interests such as operational monitoring, flood warning, reser-  
147 voir management, agricultural or environmental application.

148 In an attempt to overcome the limitations identified in the previous paragraphs,  
149 this study undertakes a global-scale analysis of the joint historical variability of floods  
150 and heavy precipitation, with the following main objectives:

- 151 1. Analyze a long 100-year period, and evaluate whether the detected trend and per-  
152 sistence components differ from those identified in the literature.
- 153 2. Provide a 180-year reconstruction of probabilities of occurrence at precipitation/streamflow  
154 stations, with a global extent.

155 To achieve these objectives, this study uses a probabilistic model belonging to the  
156 recently-developed Hidden Climate Indices framework (Renard et al., 2021). HCIs are  
157 used in a similar way to standard climate indices such as Nino 3.4 or NAO (among many  
158 others) to explain the temporal variability of data. An important difference, however,  
159 is that HCIs are not predefined time series but instead are inferred from the data. They  
160 are conceptually similar to the principal components extracted from a space-time dataset  
161 using Principal Component Analysis (also known as Empirical Orthogonal Functions anal-  
162 ysis, e.g. Hannachi et al., 2007).

163 A key strength of this HCI-based model is that it allows analyzing floods and heavy  
164 precipitation jointly, and distinguishing between: (i) trend and persistence components  
165 that affect both floods and heavy precipitation, and (ii) components that are specific to  
166 only one of them. The model also handles varying data availability and does not rely on  
167 predefined geographical regions. The joint analysis of floods and heavy precipitation over  
168 a long period (objective 1) constitute the first innovation, as illustrated by Table 1. The  
169 180-year reconstruction (objective 2) is also innovative, since no similar global-extent re-  
170 constructions of extreme probabilities computed at the scale of stations exist as far as  
171 our knowledge goes.

The remainder of this paper is organized as follows. Section 2 describes the precipitation, streamflow and atmospheric datasets. Section 3 describes the models used for analyzing floods and heavy precipitation and for reconstructing their probabilities of occurrence from atmospheric variables (pressure, wind and temperature). Results for the 100-year analysis and the 180-year reconstruction are described in Section 4. Section 5 compares the main findings of this analysis with literature results, and discusses limitations and avenues for future work. Finally, the concluding Section 6 summarizes the key insights from this work.

## 2 Data

### 2.1 Precipitation

Precipitation data are taken from HadEX2 (Donat et al., 2013) and its successor HadEX3 (Dunn et al., 2020) datasets, which are reference global-scale datasets for detecting changes in temperature and precipitation extremes (see IPCC, 2021, Chapter 11). HadEX datasets exist in two versions. The ‘station’ dataset contains time series of extreme indices derived from daily station measurements, for instance the time series of monthly maxima of daily precipitation (Rx1day). The ‘gridded’ dataset is a spatial interpolation of these extreme indices on a regular grid. The ‘station’ dataset is used in this work to avoid any smoothing effect induced by spatial interpolation and any temporal inhomogeneity induced by the varying number of available stations. Statistical analyses are based on seasonal maxima of daily precipitation, with the four seasons being defined as DJF, MAM, JJA and SON. The time series associated with each season is analyzed separately.

A subset of 1721 stations from HadEX datasets is used (Figure 1). The selection procedure is described in detail in the Supporting Information Text S1, and can be broadly summarized as follows:

1. Remove stations with less than 20 years of data: a higher threshold would result in many stations from Africa and South-East Asia being excluded from the study.
2. Remove stations containing suspicious outliers (see Supporting Information Text S1 for details).

Reference	Var. <sup>a</sup>	Extent	# stations × period	Key findings
Papalexiou & Montanari (2019)	P	Global <sup>b</sup>	8730 × 1964-2013	Overall increase in frequency
Dunn et al. (2020)	P	Global	gridded <sup>c</sup> × 1950-2018	Overall increase, with regional differences
Q. Sun et al. (2021)	P	Global	7293 × 1950-2018 or 1974 × 1900–2018	Significant increases dominate, with regional differences
Hodgkins et al. (2017)	Q	Europe and North America	1204 × 1961-2010 or 322 × 1931–2010	No compelling evidence for increase in major floods
Blöschl, Hall, et al. (2019)	Q	Europe	3738 × 1960-2010	Region-dependent, with both increases and decreases
Gudmundsson et al. (2019)	Q	Global	(≈ 7000) × (40-year periods in 1951-2010)	Region-dependent, with both increases and decreases
This article	P & Q	Global	3141 × 1916-2015	See Section 6

**Table 1.** Properties of large-scale analyses of floods and heavy precipitation for a few selected recent references.

<sup>a</sup> Variable: P for heavy precipitation, Q for floods.

<sup>b</sup> data are available on all continents (Antarctica excluded) but density may strongly vary.

<sup>c</sup>  $1.875^\circ \times 1.25^\circ$  longitude-latitude grid.

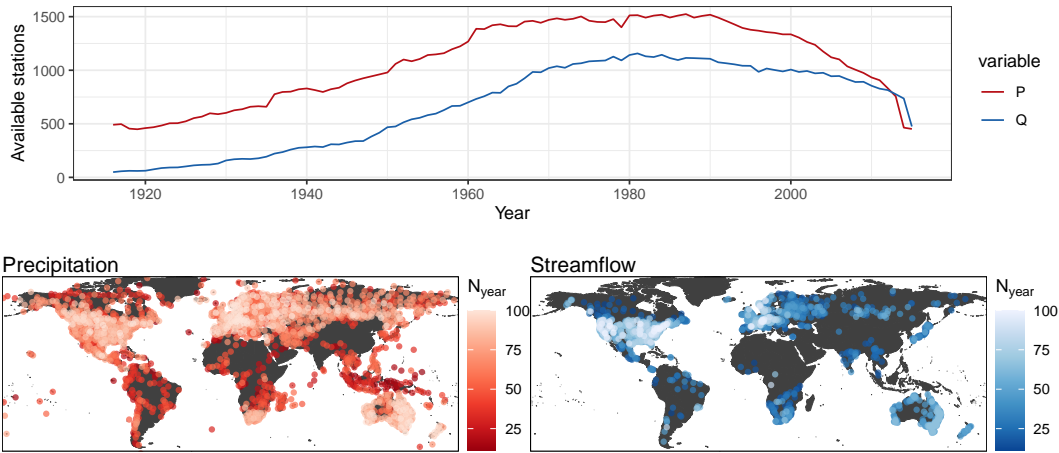


**Figure 1.** Data availability: evolution of the number of precipitation (P) and streamflow (Q) stations (top) and maps of their location (bottom). The figure shows all selected stations as described in Sections 2.1 (P, 1721 stations) and 2.2 (Q, 1420 stations). Note however that the number of stations effectively used in each of the four seasonal analyses will be smaller due to the season-specific constraint described in Section 3.2.1. Zoomable versions of these maps are available online at <https://hydroapps.recover.inrae.fr/HEGS-paper>.

- 201 3. Remove sets of stations sharing more than 10% of identical non-zero values: these
- 202       are likely affected by an infilling procedure used in some countries where a single
- 203       series is used to infill many others.
- 204 4. Merge HadEX2 and HadEX3 by favoring the HadEX3 version whenever a station
- 205       appears in both datasets: this allows preserving large parts of South America, Africa
- 206       and Southeast Asia that had data in HadEX2 but not in HadEX3.
- 207 5. Apply spatial subsampling by selecting the single longest station in a  $2 \times 2$  de-
- 208       grees box: this reduces large inhomogeneities in the spatial density of stations and
- 209       makes their number more computationally manageable for the same global cov-
- 210       erage.

## 211 2.2 Streamflow

212 Streamflow data are taken from the GSIM dataset (Do et al., 2018; Gudmundsson  
 213 et al., 2018b), which contains time series of streamflow indices (e.g. monthly mean, min  
 214 and max) at more than 30,000 stations worldwide. GSIM includes the GRDC dataset,

which has been frequently used in large-scale hydrologic analyses (Global Runoff Data Centre, 2015), as well as 11 regional or national datasets. As for precipitation, statistical analyses are based on time series of seasonal (DJF, MAM, JJA, SON) maxima of daily streamflow, with the four seasons being treated separately.

GSIM is probably the most complete streamflow dataset in terms of spatial coverage, but it includes highly regulated catchments that are not suited to the analysis of climate-driven variability. The usual approach to avoid this challenge is to use ‘Reference Hydrologic Networks’ (RHN, Whitfield et al., 2012; Burn et al., 2012), but RHNs are restricted to a few countries and do not have, to date, a global extent. In order to favor RHN or RHN-like stations while preserving the global extent of the GSIM dataset, the following strategy for selecting stations is implemented:

1. In countries where a known RHN exists, only GSIM stations belonging to the RHN are used. This applies to the European and North-American countries studied in the flood trend analysis of Hodgkins et al. (2017), plus Australia (Bureau of Meteorology, 2020) and Brazil.
2. In countries that do not have a known RHN, stations are selected using GSIM metadata (series length and homogeneity, missing value rate, reliability of catchment delineation, population density, total dam volume and land cover type).
3. For France and Australia, GSIM data are replaced with a more recent version of the RHN datasets: this allows improving space and time coverage and, in the case of Australia, to resolve an issue linked to the handling of quality flags (Gudmundsson et al., 2018a).
4. As for precipitation, spatial subsampling is implemented but with a 0.5 degrees grid box.

This selection procedure results in the subset of 1420 stations shown in Figure 1. The Supporting Information Text S2 provides more details on this procedure, and in particular on the metadata-based criteria used in point 2 to judge the ‘RHN-ness’ of stations in countries with no formal RHN.

243        **2.3 Atmospheric Variables**

244        In this work, atmospheric variables are used as predictors to reconstruct flood and  
 245        heavy precipitation probabilities in the distant past. Two long reanalysis products can  
 246        be used for this purpose: the ERA-20C (Poli et al., 2016) and the 20th Century (20CR,  
 247        Compo et al., 2011) reanalyses. We opted for the latter in its third version (20CRv3, Slivin-  
 248        ski et al., 2019) because it is an ensemble reanalysis, with multiple members represent-  
 249        ing uncertainty, and it also starts earlier (1836 vs. 1900 for ERA-20C).

250        Four variables are used in this study: temperature, zonal and meridional wind com-  
 251        ponents at 850 hPa (T850, U850, V850) and mean sea level pressure (PRMSL). For each  
 252        variable, data are averaged over the season of interest and subsampled on a 2.8125 de-  
 253        gree grid (1/4 of the original resolution) to avoid unnecessary storage and computing time  
 254        issues. The 80 individual members provided by 20CRv3 to represent uncertainty are used  
 255        rather than the ensemble mean ([https://portal.nersc.gov/archive/home/projects/  
incite11/www/20C\\_Reanalysis\\_version\\_3/](https://portal.nersc.gov/archive/home/projects/incite11/www/20C_Reanalysis_version_3/), accessed January 2022). These variables  
 256        were chosen because they are frequently used to study large-scale climate variability and  
 257        derive climate indices. Likewise, seasonal averaging is frequently applied when using climate-  
 258        informed models for floods or heavy precipitation (e.g. X. Sun et al., 2015; Lee et al., 2018).  
 259        However, we note that alternative choices could be made on both aspects: this will be  
 260        further discussed in Section 5.4.  
 261

262        **3 Methods**

263        The study methodology uses two probabilistic models to implement three main tasks  
 264        as summarized in Figure 2. We start by providing a short and intuitive introduction to  
 265        the HCI modeling framework upon which the two probabilistic models are built, refer-  
 266        ring to Renard & Thyre (2019) and Renard et al. (2021) for an in-depth description of  
 267        technical aspects. We then describe the three tasks implemented in this work. The first  
 268        task analyses the precipitation+streamflow dataset in order to identify a set of HCIs that  
 269        drive their temporal variability (Model 1). In the second task, the effects of the same  
 270        HCIs on atmospheric variables are estimated (Model 2). Finally, the third task uses these  
 271        two models to reconstruct flood and heavy precipitation probabilities from atmospheric  
 272        data.

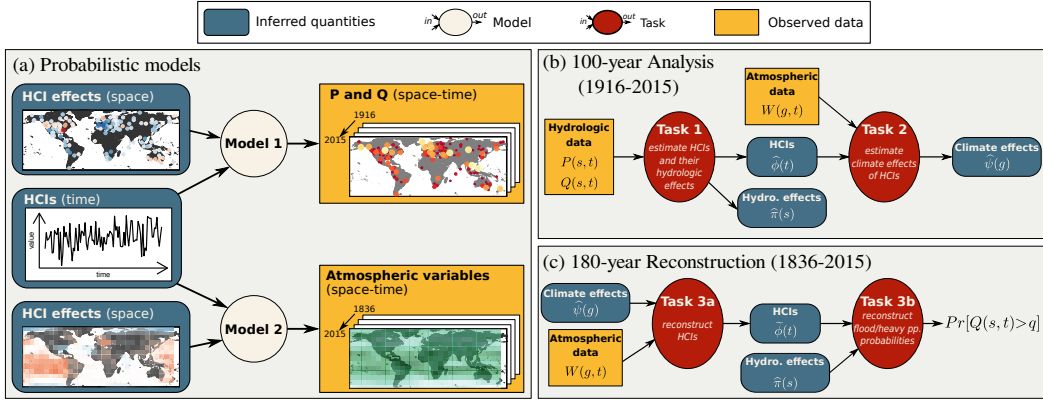


**Figure 2.** Methodological overview. (a) Two probabilistic models used in this study for describing hydrologic extremes (floods and heavy precipitation) and atmospheric variables (pressure, wind, temperature). Note that the two models share the same Hidden Climate Indices (HCIs) as input. (b) Tasks applied to implement the 100-year analysis; (c) Tasks applied to perform the 180-year reconstruction.

273

### 3.1 A Short Introduction to HCI modeling

274

Consider a space-time dataset such as the one shown in Figure 3a, representing standardized streamflow anomalies at  $S = 42$  stations during  $T = 45$  years (1970-2014, see Renard & Thyre, 2019). Let  $Y(s, t)$  denote the random variable generating the observation at site  $s$  and time  $t$ . A common way to describe the temporal variability of such data is to use a linear regression to model the influence of a time-varying covariate  $\tau(t)$  at each site:

275

276

277

278

279

$$Y(s, t) = \lambda(s)\tau(t) + \varepsilon(s, t), \text{ with } \varepsilon(s, t) \sim \mathcal{N}(0, \sigma(s)) \quad (1a)$$

$$\text{or equivalently: } Y(s, t) \sim \mathcal{N}(\lambda(s)\tau(t), \sigma(s)) \quad (1b)$$

280

281

282

283

284

285

A climate index such as Nino 3.4, for instance, is often used as the covariate  $\tau(t)$ .

However, it is also possible to consider that the climate index is *hidden* by treating it as an unknown time series that needs to be inferred from the data. This cannot be achieved at a single site because the number of datapoints ( $T$ ) is smaller than the number of unknown quantities ( $T + 2$ ). However, inference becomes feasible when all sites are con-

286 sidered together, since the number of datapoints ( $T \times S$ ) becomes large compared with  
 287 the number of unknowns ( $T + 2S$ ).

288 The Gaussian HCI model of Equation (1) is closely related to Principal Compo-  
 289 nent Analysis (PCA), as shown by Tipping & Bishop (1999). As an illustration, Figure 3b  
 290 shows the estimated HCI  $\hat{\tau}(t)$  (as described in Renard et al., 2021), and compares it with  
 291 the first component of a standard PCA applied to the same data: the two time series  
 292 are nearly identical. PCA therefore provides a convenient analogy to interpret the out-  
 293 comes of an HCI model: the estimated HCI time series  $\hat{\tau}(t)$  can be thought of as the prin-  
 294 cipal component driving the temporal variability of the dataset. The associated spatial  
 295 parameters  $\hat{\lambda}(s)$  (Figure 3c, called ‘effects’ in statistical terminology) are similar to PCA  
 296 loadings and control the strength of the HCI influence at each site: data from sites where  
 297  $\hat{\lambda}(s)$  is large closely follow the HCI  $\hat{\tau}(t)$  (or its opposite if  $\hat{\lambda}(s)$  is negative), while data  
 298 from sites where  $\hat{\lambda}(s) \approx 0$  follow an unrelated pattern.

299 While the similarity with PCA is convenient for interpretation, we stress that HCI  
 300 modeling has important advantages over PCA that will be exploited in this work:

- 301 1. It is based on an explicit probabilistic model, which provides a natural framework  
     302 to make probabilistic predictions.
- 303 2. Probabilistic assumptions such as the regression formula or the normality assump-  
     304 tion in Equation (1) can be modified as needed.
- 305 3. The treatment of missing values is straightforward with likelihood and Bayesian  
     306 estimation methods (Renard et al., 2021) and does not require infilling; this is par-  
     307 ticularly useful for the datasets shown in Figure 1.
- 308 4. Additional probabilistic assumptions can be made to model the time series  $\tau(t)$   
     309 (e.g. trend, autocorrelation) and the spatial process  $\lambda(s)$  (e.g. spatial correlation).

### 310   **3.2 Step 1: Identifying HCIs from Precipitation and Streamflow Data**

#### 311    **3.2.1 Expressing Data as Nonexceedance Probabilities**

312 Raw series of seasonal maxima are expressed in  $mm$  (P) or  $m^3.s^{-1}$  (Q), and in the  
 313 case of streamflow they may vary by several orders of magnitude between sites. The usual  
 314 approach of expressing streamflow in  $mm$  cannot be applied because catchment areas  
 315 are unreliable for a non-negligible fraction of the dataset (see Do et al., 2018, for details

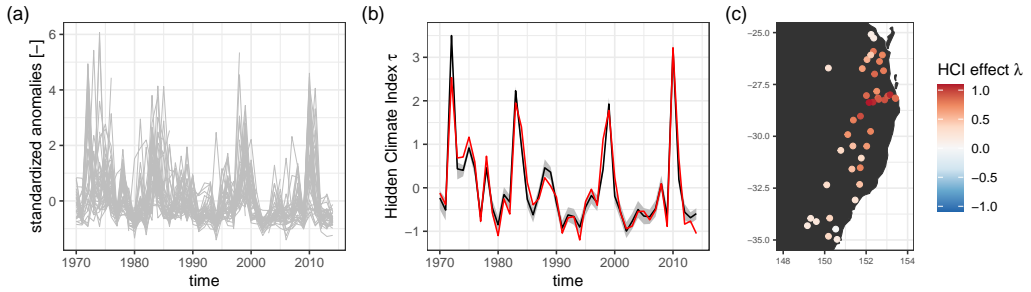


**Figure 3.** Illustration of a simple Hidden Climate Index (HCI) model and its relationship with Principal Component Analysis (PCA). (a) Standardized streamflow anomalies during the austral spring (SON) at 42 stations in Eastern Australia (one line per station). (b) Estimated HCI  $\hat{\tau}(t)$  (black line) and 90% uncertainty interval (gray area). The red line is the standardized first component of a PCA applied to the same data. (c) Effect of the HCI at each site  $\hat{\lambda}(s)$ .

on this issue). Some form of standardization is therefore desirable to facilitate the derivation of a spatial model. Given the focus on extremes, we decided to consider the return period associated with each seasonal maxima, or equivalently but more conveniently, to transform seasonal maxima into nonexceedance probabilities (Figure 4). This is achieved at each site as follows:

1. Extract the time series of annual maxima.
2. Estimate a Generalized Extreme Value (GEV) distribution using the L-Moment method.
3. Apply the cumulative distribution function (cdf) of this estimated GEV to seasonal maxima.

Note that the GEV is estimated using annual maxima, but is applied to seasonal maxima. Consequently, nonexceedance probabilities will all be close to zero at a station where extremes never occur during the considered season, as illustrated in Figure 4(b). An additional constraint is used to avoid such situations which are not representative of floods or heavy precipitation: at a given station, at least one probability value should exceed 0.8 (i.e. at least one 5-year event should have occurred during the season). If this does not hold, the station is removed from the analysis for this season. This brings the number of stations effectively used in the analyses to 1406 (P) and 818 (Q) for SON, 947

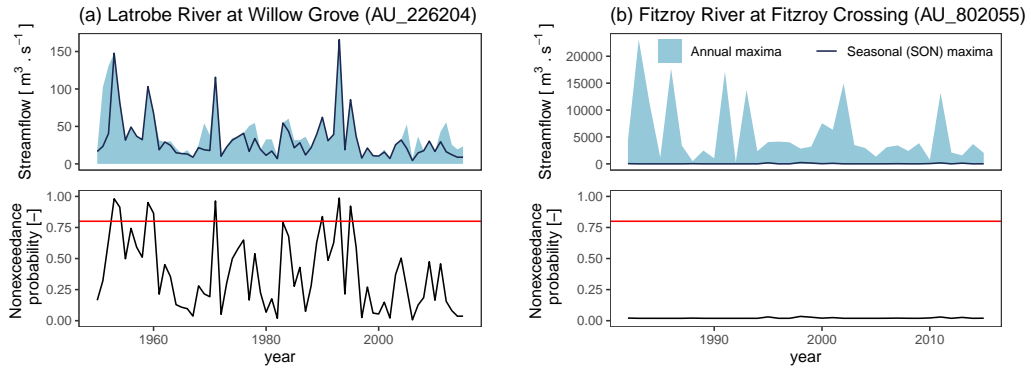


**Figure 4.** Illustration of the transformation from raw data to nonexceedance probabilities using two Australian streamflow stations. In case (a), the maximum daily streamflow during the SON season (line) often coincides with the annual maximum (shaded area). This indicates that floods often occur during the SON season at this station, leading nonexceedance probabilities to exceed the 0.8 threshold (red line). By contrast, no floods occur during the SON season in case (b), and as a result, all probabilities are well below the 0.8 threshold: this station will therefore be excluded from the analysis for the SON season.

334 (P) and 834 (Q) for DJF, 1219 (P) and 1179 (Q) for MAM, 1406 (P) and 881 (Q) for  
335 JJA.

336 The use of probability-transformed values does not constitute a limitation in the  
337 context of this work. Indeed, the physical values (in  $mm$  or  $m^3 \cdot s^{-1}$ ) taken by extreme  
338 events at stations strongly depend on local factors (e.g. windward / leeward location for  
339 P, catchment size for Q), but probability-transformed values are sufficient to study the  
340 regional covariability of extremes and its modulation by the large-scale climate. Besides,  
341 nonexceedance probabilities can always be transformed back into  $mm$  (P) or  $m^3 \cdot s^{-1}$  (Q)  
342 by applying the quantile function of the estimated GEV distribution.

### 343 3.2.2 HCI Model

344 The model described in this section applies to data for one given season, and will  
345 be used four times to separately analyze SON, DJF, MAM and JJA. Let  $P(s, t)$  and  $Q(s, t)$   
346 denote precipitation and streamflow data at site  $s$  and time  $t$ , expressed as nonexceedance  
347 probabilities as described in the previous section. A natural distribution for such data

348 belonging to the interval (0;1) is the Beta distribution  $Beta(a, b)$ , where  $a$  and  $b$  are two  
 349 shape parameters. In this work, a reparameterized version  $Beta(\mu, \nu)$  is favored, where  
 350  $\mu \in (0; 1)$  is the mean and  $\nu > 0$  is a concentration parameter (the larger  $\nu$ , the smaller  
 351 the variance). This reparameterized version makes the model more convenient to build  
 352 and use since mean/concentration parameters are easier to interpret than shape param-  
 353 eters. The formulas to move between parameterizations are the following:

$$\begin{cases} \mu = a/(a+b) \\ \nu = a+b \end{cases} \iff \begin{cases} a = \mu\nu \\ b = (1-\mu)\nu \end{cases} \quad (2)$$

354 Precipitation and streamflow data are then assumed to be realizations from Beta  
 355 distributions whose parameters vary in space and time as follows:

Distributions of  $P$  and  $Q$ : 
$$\begin{cases} P(s, t) \sim Beta(\mu_P(s, t), \nu_P(s, t)) \\ Q(s, t) \sim Beta(\mu_Q(s, t), \nu_Q(s, t)) \end{cases} \quad (3a)$$

Space-time model for  $\mu$ : 
$$\begin{cases} logit(\mu_P(s, t)) = \zeta_{\mu_P}(s) + \sum_{k=1}^K \lambda_{k,P}(s)\tau_k(t) + \sum_{k=1}^K \theta_{k,P}(s)\delta_k(t) \\ logit(\mu_Q(s, t)) = \zeta_{\mu_Q}(s) + \sum_{k=1}^K \lambda_{k,Q}(s)\tau_k(t) + \sum_{k=1}^K \theta_{k,Q}(s)\omega_k(t) \end{cases} \quad (3b)$$

Space model for  $\nu$ : 
$$\begin{cases} log(\nu_P(s, t)) = \zeta_{\nu_P}(s) \\ log(\nu_Q(s, t)) = \zeta_{\nu_Q}(s) \end{cases} \quad (3c)$$

356

357 Equation (3) can be interpreted as a generalization of the simple HCI model of Equa-  
 358 tion (1b), using a different distribution (Beta rather than Gaussian) and more complex  
 359 regression formulas. Equation (3b) describes how the mean of precipitation and stream-  
 360 flow data varies in space and time and is at the core of the model. The *logit* transfor-  
 361 mation is used to ensure that the mean remains in the interval (0;1). For each variable,  
 362 the first term ( $\zeta_{\mu_P}(s)$  or  $\zeta_{\mu_Q}(s)$ ) is a site-specific constant (a.k.a. intercept). The sec-  
 363 ond term models time variability by means of a set of  $K$  HCI time series  $\tau_k(t)$ . The ef-  
 364 fect of these HCIs at each site is controlled by a set of  $K$  spatial processes ( $\lambda_{k,P}(s)$  or  
 365  $\lambda_{k,Q}(s)$ ). Importantly, the same time series  $\tau_k(t)$  are used for both  $P$  and  $Q$  variables:  
 366 the second term of equation (3b) therefore represents the temporal variability common

367 to  $P$  and  $Q$ . By contrast, the third term models time variability in a similar way but uses  
 368 distinct time series  $\delta_k(t)$  and  $\omega_k(t)$  for  $P$  and  $Q$ , respectively. This third term therefore  
 369 represents the temporal variability specific to  $P$  or  $Q$ . Finally, equation (3c) states that  
 370 the concentration parameters vary in space but not in time, with the *log* transformation  
 371 ensuring they remain positive.

372 In addition, it is assumed that any spatial or temporal dependence in precipitation  
 373 and streamflow, or any cross-dependence between them, is induced by the HCIs and their  
 374 effects. In statistical terms, this corresponds to making an assumption of conditional in-  
 375 dependence. We refer to Renard et al. (2021) for a thorough analysis of this assumption  
 376 and its consequences, but one important point in the context of this work is that con-  
 377 ditional independence makes the treatment of missing values straightforward: datasets  
 378 presenting highly irregular availability, such as those in Figure 1, can hence easily be ac-  
 379 commodated.

380 Model specification is completed with additional assumptions on the time and space  
 381 variability of HCIs and their effects. Starting with the latter, all spatial processes in equa-  
 382 tion (3) are assumed to follow Nearest-Neighbor Gaussian Processes (NNGP, Datta et  
 383 al., 2016a). Using the generic notation  $\boldsymbol{\pi} = (\pi(s))_{s=1:S}$  to denote any of the spatial pro-  
 384 cesses in equation (3) ( $\zeta$ 's,  $\lambda$ 's or  $\theta$ 's):

$$\left\{ \begin{array}{l} \boldsymbol{\pi} \sim NNGP(\mathbf{m}, \mathbf{V}) \\ m_i = \alpha, \forall i = 1 \dots S \\ V_{i,j} = \eta_0^2 \exp(-d_{i,j}/\eta_1) \quad \forall i, j = 1 \dots S \end{array} \right. \quad (4)$$

385 Equation (4) corresponds to a constant-mean process with intersite covariance de-  
 386 creasing exponentially as a function of intersite distance. The NNGP is essentially a stan-  
 387 dard Gaussian Process that has been modified to make it computationally tractable with  
 388 a large number of sites. It does so by avoiding the need to use the whole covariance ma-  
 389 trix  $\mathbf{V}$  (whose inversion/multiplication involves  $\mathcal{O}(n^3)$  operations), replacing it by the  
 390 use of many smaller  $m \times m$  matrices representing covariances between the  $m$  nearest neigh-  
 391 bors of each site ( $m = 5$  is used in this study). We refer to the papers by Datta et al.  
 392 (2016a,b) and Banerjee (2017) for technical details.

393 Similar to the spatial effects, all HCI time series are assumed to follow NNGPs. Us-  
 394 ing as previously a generic notation  $\phi = (\phi(t))_{t=1:T}$  to denote any of the HCI time se-  
 395 ries in equation (3) ( $\tau$ 's,  $\delta$ 's or  $\omega$ 's):

$$\begin{cases} \phi \sim NNGP(\mathbf{m}, \mathbf{V}) \\ m_i = \beta \left( i - \frac{T}{2} \right), \forall i = 1 \dots T \\ V_{i,j} = \gamma_0^2 \exp(-|i-j|/\gamma_1) \quad \forall i, j = 1 \dots T \end{cases} \quad (5)$$

396 Two parameters are of particular interest in equation (5) and will be specifically  
 397 monitored in the results:  $\beta$  represents a trend affecting the HCI, while  $\gamma_1$  controls its au-  
 398 tocorrelation (the lag-1 autocorrelation is equal to  $e^{-1/\gamma_1}$ ). The latter can be used to de-  
 399 tect the existence of low-frequency variability (extreme-rich, extreme-poor periods). It  
 400 is noted that many alternative models could be used to describe low-frequency variabil-  
 401 ity (Henley et al., 2011), but the simple model of equation (5) is considered fit for the  
 402 purpose of first detecting its existence.

### 403 3.2.3 Inference

404 The model described in Section 3.2.2 requires estimating the intercepts  $\zeta$ , the HCIs  
 405  $\boldsymbol{\tau}$ ,  $\boldsymbol{\delta}$ ,  $\boldsymbol{\omega}$  and their effects  $\boldsymbol{\lambda}$ ,  $\boldsymbol{\theta}$  along with the parameters of their hyper-distributions  $\boldsymbol{\alpha}$ ,  
 406  $\boldsymbol{\eta}_0$ ,  $\boldsymbol{\eta}_1$ ,  $\beta$ ,  $\gamma_0$  and  $\gamma_1$ . This is achieved by deriving the posterior distribution of these un-  
 407 known parameters and exploring it with a Monte Carlo Markov Chain (MCMC) sam-  
 408 pler. We refer to Renard & Thyer (2019) and Renard et al. (2021) for a complete tech-  
 409 nical description. In a nutshell, the key ingredients are:

- 410 1. Identifiability constraints that make the estimation of HCIs feasible: each HCI has  
   411 mean zero and variance one;
- 412 2. A stepwise approach: the model is first estimated with a single component ( $K =$   
   413 1 in equation (3)), yielding estimates for  $\tau_1(t)$ ,  $\delta_1(t)$  and  $\omega_1(t)$ ; the second com-  
   414 ponent ( $K=2$ ) is then estimated conditionally on the first-component estimates,  
   etc.;
- 415 3. A customized MCMC algorithm that avoids unnecessary computations.

417 Prior distributions need to be specified for hyper-parameters. For  $\boldsymbol{\eta}_1$  and  $\gamma_1$  that  
 418 control decorrelation distance and time, exponential priors with parameters 1000 km and

419 10 years, respectively, are used to set their order of magnitude. Flat priors are used for  
 420 all other hyper-parameters.

421 MCMC sampling is performed by running 40 chains in parallel, corresponding to  
 422 10 chains for each of the 4 seasons. Each chain is run for 30,000 iterations and the first  
 423 third is discarded as burn-in. Computing time is case-dependent, but as a rough order  
 424 of magnitude, 36 hours are needed to generate 30,000 MCMC samples (i.e. one chain)  
 425 on a high-performance computing cluster. This is for one step of the stepwise approach  
 426 described previously, and it therefore needs to be multiplied by the number of compo-  
 427 nents considered, which is set to  $K = 5$  in this study.

### 428 3.3 Step 2: Estimating HCI effects on Atmospheric Variables

429 Estimated HCI time series  $\hat{\tau}_k$ ,  $\hat{\delta}_k$  and  $\hat{\omega}_k$  are available for all  $k = 1 \dots K$  after  
 430 the completion of Step 1 (Section 3.2). As illustrated in Figure 2b, the next step is to  
 431 estimate their effects on the atmospheric variables described in Section 2.3 (pressure, U  
 432 and V wind and temperature). As previously, a generic notation  $\hat{\phi}_k = (\hat{\phi}_k(t))_{t=1:T}$   
 433 is used to denote any of these HCI time series. Let  $W_v(g, t)$  denote the value taken by  
 434 the  $v$ th atmospheric variable at gridpoint  $g$  and time  $t$  (belonging to the calibration pe-  
 435 riod used to estimated the HCIs). Each variable is centered and scaled to unit standard  
 436 deviation, i.e. standardized anomalies are considered. It is assumed that the space-time  
 437 variability of variables  $\mathbf{W}$  is influenced by the same HCIs as the one controlling precip-  
 438 itation and streamflow data according to the following model:

$$439 \begin{aligned} W_v(g, t) &\sim \mathcal{N}(\mu_v(g, t), \sigma_v(g)) \\ 440 \text{with } \mu_v(g, t) &= \psi_{0,v}(g) + \sum_{k=1}^K \psi_{k,v}(g) \hat{\phi}_k(t) \end{aligned} \quad (6)$$

441 For a given variable  $v$  and a given gridpoint  $g$ , this equation is a standard linear  
 442 regression model, which allows estimating the effects  $\psi$  using standard regression for-  
 443 mulas. More precisely, let  $\mathbf{w}$  denote observations of the atmospheric variables for the  $T$   
 444 calibration time steps, arranged in a matrix with  $T$  rows and  $G \times V$  columns (this as-  
 445 sumes that all  $V$  variables are observed on the same spatial grid of size  $G$ , but this can  
 easily be generalized). Moreover let the estimated HCIs be arranged in a  $T \times (K + 1)$   
 matrix  $\mathbf{T}$  as follows:

$$\Upsilon = \begin{pmatrix} 1 & \hat{\phi}_1(t_1) & \dots & \hat{\phi}_K(t_1) \\ \vdots & \vdots & \vdots & \vdots \\ 1 & \hat{\phi}_1(t_T) & \dots & \hat{\phi}_K(t_T) \end{pmatrix} \quad (7)$$

446 Estimation of the effects  $\psi$  can then be performed using the ordinary least square  
 447 estimator:

$$\left( \underbrace{\hat{\psi}_0, \hat{\psi}_1, \dots, \hat{\psi}_K}_{GV \times (K+1)} \right)^T = \underbrace{(\Upsilon^T \Upsilon)^{-1}}_{(K+1) \times (K+1)} \times \underbrace{\Upsilon^T}_{(K+1) \times T} \times \underbrace{\mathbf{w}}_{T \times GV} \quad (8)$$

448 Note that the formula in equation (8) applies to observed atmospheric variables  
 449  $\mathbf{w}$ . However, as explained in Section 2.3, the 20CRv3 reanalysis provides 80 realizations  
 450 of atmospheric variables  $\mathbf{w}$  to represent the uncertainty affecting the reanalysis. This  
 451 uncertainty can be propagated forward to the effects  $\psi$  by simply reapplying equation (8)  
 452 to each of the 80 realizations.

### 453 3.4 Step 3: Reconstructing Flood and Heavy Precipitation Probabil- 454 ities from Atmospheric Variables

455 As illustrated in Figure 2c, the objective of this third step is to use the atmospheric  
 456 variables described in Section 2.3 to reconstruct the HCI time series which, in turn, can  
 457 be used to estimate flood and heavy precipitation probabilities using the HCI model of  
 458 Step 1. This is of particular interest to extend the analysis period from 1916-2015 to 1836-  
 459 2015.

460 For a particular time step  $t^*$ , the task is therefore to estimate the HCIs  $\phi^*$  using  
 461 atmospheric data  $\mathbf{w}^*$ . Equation (6) can once again be used for this purpose, but in an  
 462 ‘inverted’ setup: effects  $\hat{\psi}$  are known from equation (8) and HCIs  $\phi^*$  are sought, which  
 463 is the opposite of step 2. Since standard deviations  $\hat{\sigma}_v(g)$  have also been estimated in  
 464 the previous step, a weighted least square estimator can be used to compute the recon-  
 465 structed  $\tilde{\phi}^*$ :

$$\tilde{\phi}^* = (\tilde{\phi}_1(t^*), \dots, \tilde{\phi}_K(t^*))^T = \underbrace{(\hat{\Psi}^T \hat{\Omega} \hat{\Psi})^{-1}}_{K \times K} \times \underbrace{\hat{\Psi}^T}_{K \times GV} \times \underbrace{\hat{\Omega}}_{GV \times GV} \times \underbrace{(\mathbf{w}^* - \hat{\psi}_0)}_{GV \times 1} \quad (9)$$

466 where  $\hat{\Omega}$  is a  $GV \times GV$  matrix containing  $1/\hat{\sigma}_v^2(g)$  on its diagonal and  $\hat{\Psi}$  is defined in  
 467 equation (8). The reconstructed  $\tilde{\phi}^*$  can then be used in the HCI model of equation (3)  
 468 to reconstruct the distribution of  $P$  and  $Q$  and any related quantities (e.g. probability  
 469 of exceeding some threshold, task 3b in Figure 2c). As previously, this process can be  
 470 repeatedly applied to the 80 20CRv3 members to propagate the associated uncertainty.

## 471 4 Results

472 This section follows the steps outlined in Figure 2. HCI time series and their spa-  
 473 tial effects are first identified from  $P$  and  $Q$  data and their properties are described. The  
 474 effects of these HCIs on atmospheric variables are then estimated, and the associated re-  
 475 gression model is finally used to reconstruct flood and heavy precipitation distributions  
 476 since 1836. The latter analysis also includes an assessment of the reliability and sharp-  
 477 ness of the probabilistic reconstructions using a cross-validation exercise. Detailed re-  
 478 sults are shown only for the SON season in the paper. Results for other seasons are avail-  
 479 able through an online app <https://hydroapps.recover.inrae.fr/HEGS-paper> (see  
 480 also Section 7) and are only summarized herein.

### 481 4.1 Hidden Climate Indices

#### 482 4.1.1 MCMC convergence

483 MCMC convergence is assessed with the Gelman-Rubin (GR) criterion (Gelman  
 484 & Rubin, 1992) and by visualizing MCMC traces (not shown). For most inferred quan-  
 485 tities, the GR criterion is well below 1.2 and the MCMC traces show that the chains are  
 486 mixing well, indicating good convergence. Overall, convergence is much faster for the  $P$ -  
 487 specific HCIs  $\delta_k(t)$  than for  $Q$ -specific and common HCIs  $\omega_k(t)$  and  $\tau_k(t)$ . Further anal-  
 488 ysis of the GR values reveals that convergence difficulties mostly pertain to HCI values  
 489  $\omega_k(t)$  and  $\tau_k(t)$  at the beginning of the period, which can be explained by the scarcity  
 490 of streamflow data prior to 1950 (Figure 1).

#### 491 4.1.2 HCIs and their effects in SON

492 Figure 5 shows the estimated HCIs and their effects for the first component (ad-  
 493 dditional components are illustrated in the online app). The  $P$ -specific HCI  $\delta_1$  shows a  
 494 slight decreasing trend (the 90% interval for  $\beta$  does not contain zero) but no strong au-

tocorrelation. Its effects are concentrated in central North America and are mostly negative: high values of  $\delta_1$  are hence associated with lower-than-usual heavy precipitation in this area. Note that the decreasing trend should be interpreted in relation to the sign of HCI effects: here the combination of a decreasing HCI trend and negative effects translates into increasing heavy precipitation.

The  $Q$ -specific HCI  $\omega_1$  shows a slight increasing trend and no noticeable autocorrelation. Its effects reveal a dipole structure across the North-Atlantic: high values of  $\omega_1$  are associated with higher-than-usual floods in the Eastern US, but lower-than-usual ones in Western Europe. Note that these effects are approximately twice as large (in absolute value) as those estimated for the  $P$ -specific HCI (compare color scales in Figure 5). Given the model in equation (3b) and the fact that HCIs are standardized to unit standard deviation, this indicates that the distribution of  $Q$  may show larger temporal variations than that of  $P$ .

The common  $P+Q$  HCI  $\tau_1$  shows no strong trend or autocorrelation. It mostly affects Australia, indicating that heavy precipitation and floods are affected by a common temporal signal in this region. This shared variability suggests a close association between heavy precipitation and floods, indicating that typical confounding factors such as antecedent moisture or snowpack play a limited role during the SON season.

Finally, Figure 5 shows that uncertainty intervals around the HCIs are fairly tight, indicating that HCIs can be precisely identified from the data. For  $Q$ -specific HCI  $\omega_1$  and common  $P+Q$  HCI  $\tau_1$ , intervals are about twice larger at the beginning of the period than at the end, reflecting the strongly decreasing availability of streamflow data.

#### 4.1.3 HCI properties for all seasons

Figure 6 evaluates the existence of trend or autocorrelation in the HCIs for all seasons. Note that it makes sense to compare trend or autocorrelation values across seasons and HCIs because all HCIs have the same standard deviation equal to one (see identifiability constraints in Section 3.2.3). Marked trends are found for the  $P$ -specific HCIs. For each of the four seasons, a large trend makes one component stand out. Figure 7 shows for instance the second  $P$ -specific HCI in SON and its effects: the upward trend is indeed clearly visible, and moreover the HCI effects are widespread, suggesting that the trend affects many areas of the world. A similar observation can be made for other sea-

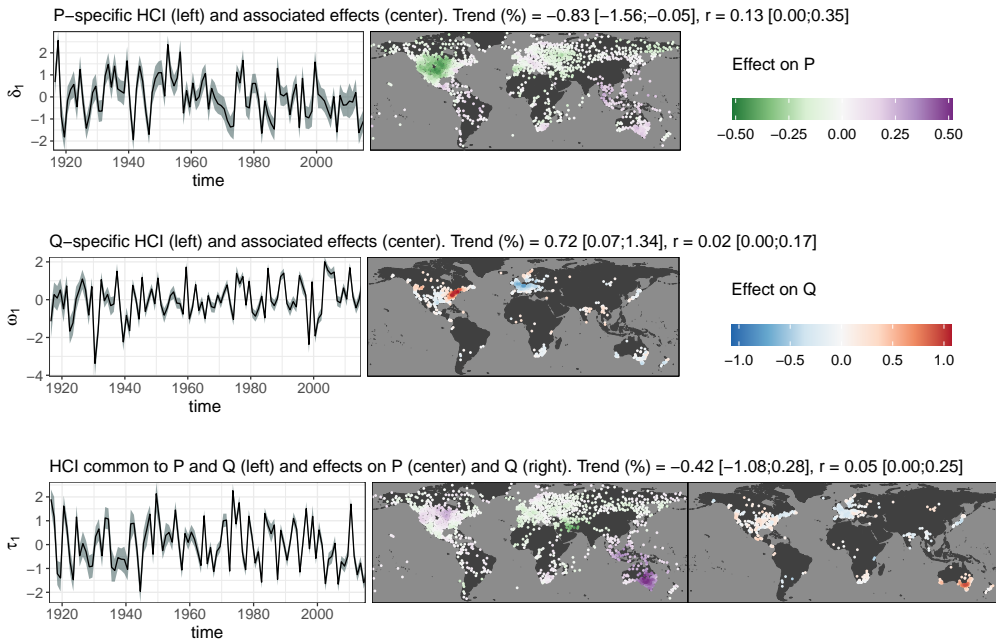


**Figure 5.** Hidden Climate Indices (HCIs) and their effects for the first component (SON season). Rows correspond to the HCI type ( $P$ -specific,  $Q$ -specific or common to  $P$  and  $Q$ ). Panels on the left show the HCI time series, with 90% posterior intervals shown in gray. Center and right panels show the associated spatial effects on  $P$  and/or  $Q$ . For each row, the title gives estimated values and 90% posterior intervals for the trend parameter  $\beta$  and the lag-1 autocorrelation  $r = e^{-1/\gamma_1}$ .

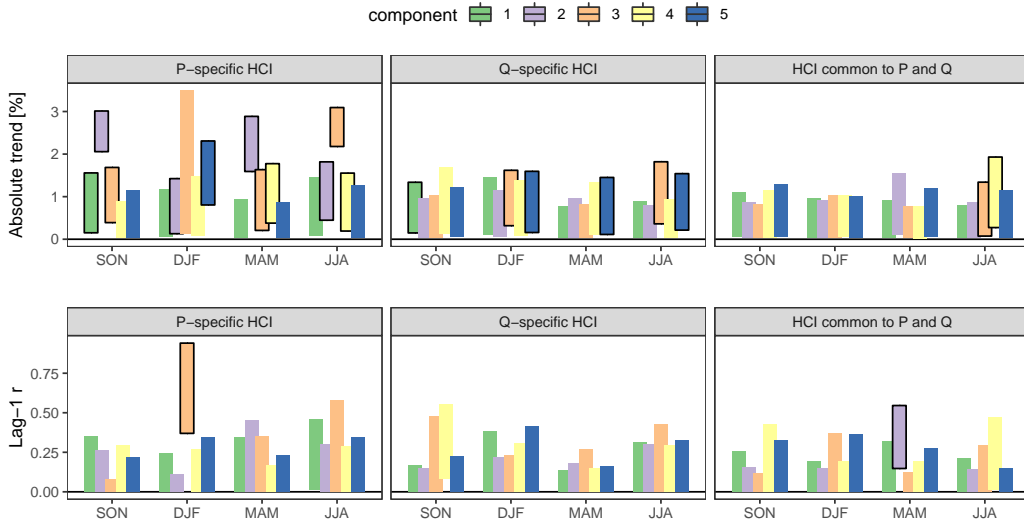


**Figure 6.** Summary of HCI properties for all 5 components and 4 seasons. Boxes denote 90% posterior intervals for the absolute trend  $|\beta|$  (top) and the lag-1 autocorrelation  $r = e^{-1/\gamma_1}$  (bottom). Outlined boxes highlight ‘large’ trends and autocorrelations, and correspond to  $\beta$ -intervals not containing 0 or  $r$ -intervals above 0.1.

sons (see online app). A few trends are found for the  $Q$ -specific HCIs, but they are much smaller than those affecting heavy precipitation, and the associated effects are also much less widespread (see online app). Finally, trends are barely noticeable for the common  $P+Q$  HCIs. Overall, these results are consistent with the literature finding that heavy precipitation shows some sign of global increase over land areas, whereas floods do not show such a consistent signal.

The bottom row of Figure 6 indicates that most HCIs do not show noticeable autocorrelation, suggesting that they represent modes of interannual, rather than low-frequency, variability. The strongest autocorrelation is detected for the third  $P$ -specific HCI during DJF, but closer inspection reveals a step-change behavior rather than a low-frequency oscillation (see online app). The second  $P+Q$  HCI in MAM also shows some moderate autocorrelation, and it mostly affects the East Coast of Australia (see online app).

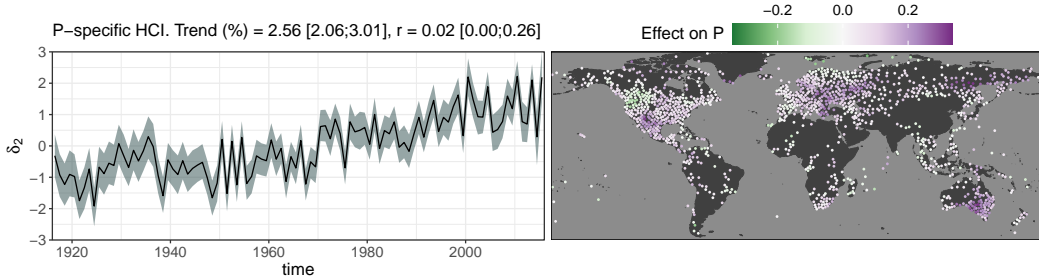


**Figure 7.** Same as Figure 5 for the  $P$ -specific HCI of the second component. This HCI is characterized by a large and wide-ranging increasing trend.

#### 538 4.2 HCI Effects on Atmospheric Variables

539 The interest in quantifying the effect of HCIs on atmospheric variables is twofold:  
 540 first, it can shed light on the origin of the HCIs, and hence on the variability of floods  
 541 and heavy precipitation, in terms of large-scale circulation; second, it sets up the regres-  
 542 sion model that will be used in Step 3 for reconstruction. Figure 8 maps the effects of  
 543 the HCIs described in Figure 5 on the four atmospheric variables (corresponding to  $\hat{\psi}_k$   
 544 in equation (8)). These effects are referred to as ‘HCI atmospheric effects’ in this sec-  
 545 tion, as opposed to the ‘HCI hydrologic effects’ that were described in Figure 5. HCI at-  
 546 mospheric effects can be compared both in space and between variables since atmospheric  
 547 variables have been centered and scaled.

548 Hydrologic effects of  $P+Q$  HCI  $\tau_1$  are essentially restricted to Australia (see Sec-  
 549 tion 4.1.2 and Figure 5), and the associated atmospheric effects shown in Figure 8 (bot-  
 550 tom row) reflect well-known drivers of floods and heavy precipitation in this region. More  
 551 precisely, strong westerly winds in the equatorial Indian Ocean, negative pressure anomaly  
 552 in the Eastern Indian Ocean and cold anomaly in the Western Indian Ocean are all typ-  
 553 ical fingerprints of the negative phase of the Indian Ocean Dipole (IOD). Likewise, the  
 554 cold anomaly pattern in the equatorial Pacific is typical of La Niña events. This single  
 555 HCI can therefore be seen as the combination of the two most influential standard cli-  
 556 mate indices in this area, namely IOD and ENSO.

557 Atmospheric effects of  $Q$ -specific HCI  $\omega_1$  (middle row) highlight well-structured pat-  
 558 terns of pressure and winds. For atmospheric pressure, the key features are widespread

positive effects over the Pacific Ocean, and a dipole over the Eastern US and Western Europe, similar to the one observed for hydrologic effects (Figure 5). The latter can be easily interpreted: high values of  $\omega_1$  are associated with positive (resp. negative) pressure anomalies over Western Europe (resp. Eastern US), and hence with less (resp. more) floods. For zonal wind, banded patterns crossing the North Atlantic may be associated with the trajectory of storms reaching Western Europe, with a similar interpretation as above (less westerly winds over Western Europe mean less floods). For meridional wind, fairly localized poles are found in the Tropical Atlantic. Since SON is the hurricane season, these may correspond to wind patterns that favor the landfall of tropical storms and hurricanes in the Eastern US.

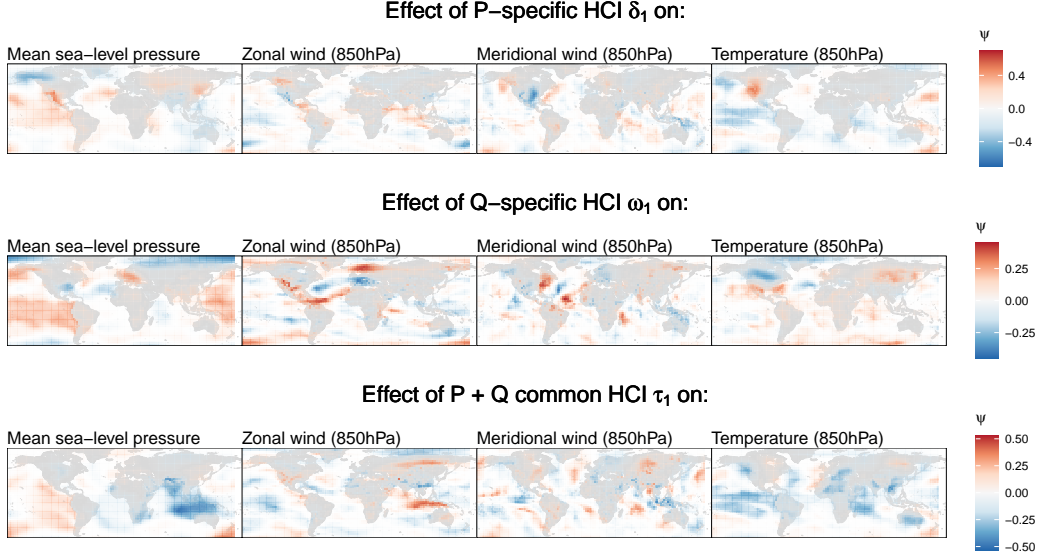
Hydrologic effects of  $P$ -specific HCI  $\delta_1$  are concentrated in the central US (Figure 5). The associated atmospheric effects (top row of Figure 8) are less clearly structured than for other HCIs and are hence more difficult to interpret. Pressure and temperature dipoles are found over Alaska and the western US. The negative anomaly in meridional wind located in the southern US may reflect the influence of moisture transport from the south (less southerly winds means less heavy precipitation in the central US). The atmospheric effects of other HCIs and other seasons are illustrated in the online app.

### 4.3 Reconstruction

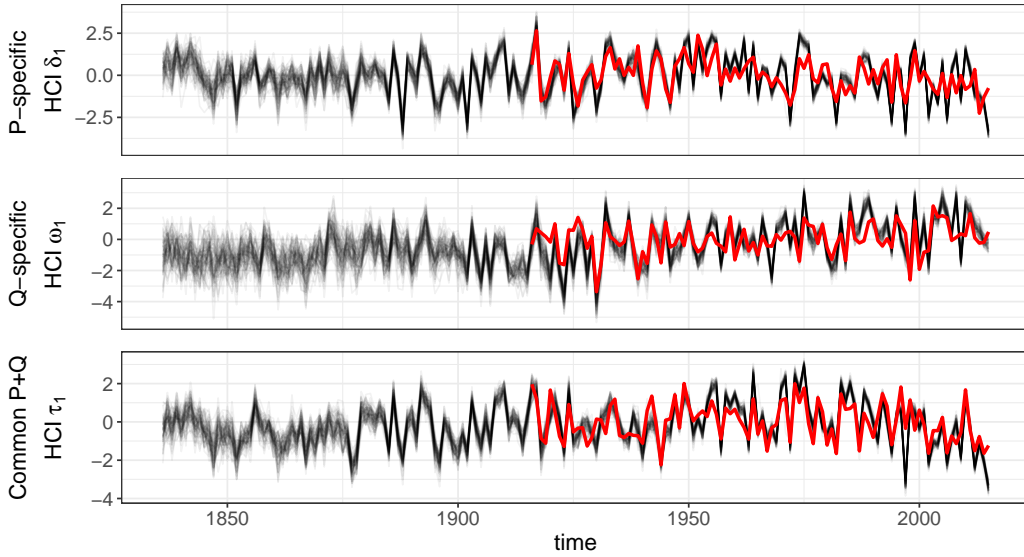
#### 4.3.1 Reconstructing Time-Varying Distributions

Figure 9 shows the HCIs reconstructed from atmospheric variables, as described in Section 3.4. Overall they are in good agreement with the HCIs that were directly estimated from  $P$  and  $Q$  data over the period 1916-2015 (average correlations: 0.71, 0.68 and 0.77 for  $\delta_1$ ,  $\omega_1$  and  $\tau_1$ , respectively). The added value of the reconstruction is that it extends back to 1836, at the cost however of an increased uncertainty: the dispersion of the 80 members of 20CRv3 is 3 to 4 times larger at the beginning of the period than at the end.

The reconstructed HCIs can then be used in the model of equation (3) to derive the time-varying distributions of  $P$  and  $Q$  over the period 1836-2015 and at all sites. Figure 10 illustrates these distributions for two sites in Australia, while the corresponding reconstructions for all sites and all seasons are released as an open dataset (see Section 7). In any given year, the variance of the distribution represents the uncertainty in the re-



**Figure 8.** Effects of Hidden Climate Indices (HCIs) on atmospheric variables for the first component (SON season). As in Figure 5, rows correspond to the HCI type ( $P$ -specific,  $Q$ -specific or common to  $P$  and  $Q$ ), columns to the atmospheric variable the effect applies to. Effects in this figure are computed with equation (8) using atmospheric data provided by the first member of the 20CRv3 reanalysis.



**Figure 9.** Hidden Climate Indices (HCIs) reconstructed from atmospheric data (pressure, wind, temperature) for the first component (SON season). In each panel, the red line corresponds to the HCI estimated from floods and heavy precipitation data (as shown in Figure 5). Each thin black line is a reconstruction based on one member of the 20CRv3 reanalysis, using equation (9).

construction, which is affected by both the uncertainty in reconstructed HCIs as discussed in the previous paragraph, but also by the uncertainty in the estimation of all spatial terms in equation (3). For the precipitation site, the time-varying distribution has a large variance, resulting in a 90% probability interval that covers an important part of the (0;1) y-axis interval (average width: 0.74). In contrast, the streamflow time-varying distribution is less uncertain (average width: 0.57), which allows highlighting years with well above-average flood probabilities: 1975 or 1992, during which major floods indeed occurred, but also 1910 or 1916, before the availability of any streamflow data at this site, or even anywhere in Australia.

The time-varying distributions can be further appraised by evaluating reliability and sharpness. Reliability is based on the Probability Integral Transform (PIT) diagram (Laio & Tamea, 2007) which evaluates the consistency between the time-varying distributions (with cdf  $F_t(x)$ ) and the observations  $o_t$  through the uniformity of PIT values  $F_t(o_t)$ . A reliability index can be computed using the area between the PIT curve shown in Figure 10 and the diagonal (Renard et al., 2010). The sharpness index is proportional to the interannual variance of the distribution's mean (Renard et al., 2021). Both indices are scaled between 0 (poor) and 1 (good).

For the precipitation site, the time-varying distribution is very reliable but not very sharp (Figure 10): it does not strongly vary between years. In contrast, the streamflow time-varying distribution is slightly less reliable but much sharper. This is a consequence of HCI effects tending to be larger for  $Q$ -specific HCIs than for  $P$ -specific ones, as discussed in Section 4.1.2. Reliability and sharpness indices at all sites are reported in Figure 11. Overall reliability indices are similar for both variables. The lack of marked spatial structures suggests that the reliability of reconstructions is similar across regions. By contrast, sharpness varies much more both spatially and between variables. Overall sharpness is markedly lower for  $P$  than for  $Q$ . Southeast Australia is the area where  $P$ -reconstructions are the sharpest, probably due to the strong influence of large-scale modes of climate variability that can be predicted from atmospheric variables. Sharpness strongly varies in space for  $Q$ -reconstructions: for instance it is much higher in Australia than in Japan, and this cannot be blamed on data availability since the station density is similar in both cases. Also note that the properties of reconstructions may also vary across seasons (not shown): for instance, during MAM and JJA, reconstructed distributions of streamflow have high reliability and sharpness in large parts of the West-

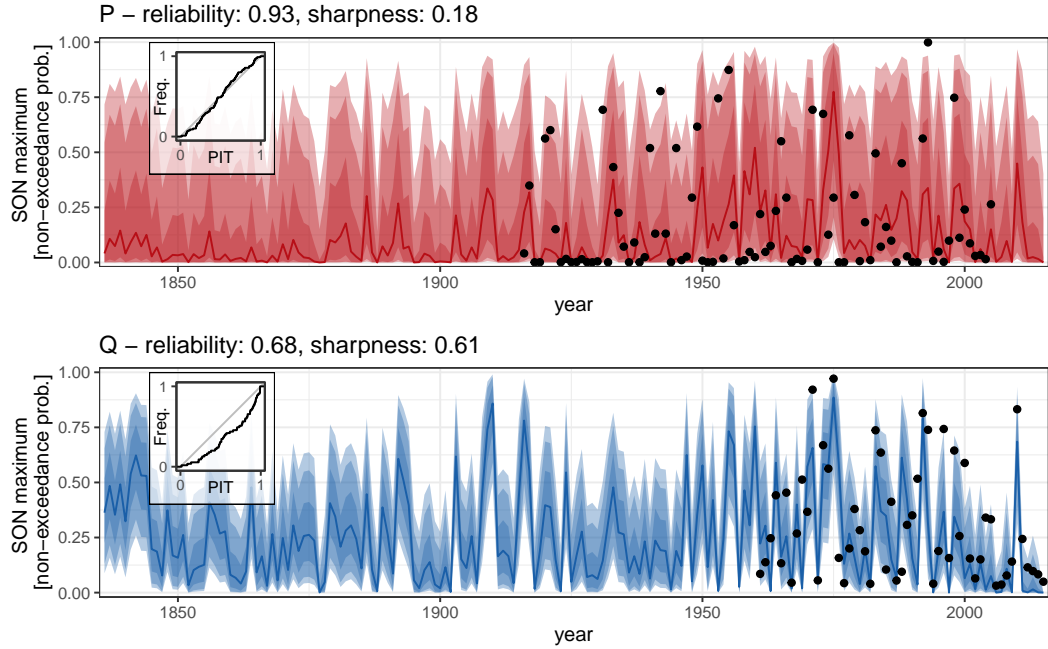


**Figure 10.** Time-varying distributions derived from reconstructed Hidden Climate Indices for one precipitation (top) and one streamflow (bottom) site, both located in Northern Victoria, Australia (SON season). The solid line denotes the median, stacked colored bands represent 50, 80 and 90% probability intervals, dots represent observed values. The title gives reliability and sharpness indices, ranging between 0 (poor) and 1 (good). The subplot panel shows the PIT diagram used to evaluate reliability (see Section 4.3.1 for details).

ern US, probably linked to snowmelt-induced flows. The sharpness of precipitation reconstructions also appears to be higher in DJF.

#### 4.3.2 Cross-Validation

A cross-validation experiment is used to complement the previous assessment of reliability and sharpness in a predictive context. The estimation sample comprises even-numbered years and is used to estimate HCI atmospheric effects (regression model used in Section 4.2). The validation sample comprises odd-numbered years and is used to compare observed values with reconstructed time-varying distributions. Figure 12 summarizes the results for both heavy precipitation and floods, with reliability and sharpness indices computed on the validation sample only, or on the full dataset as in Section 4.3.1.

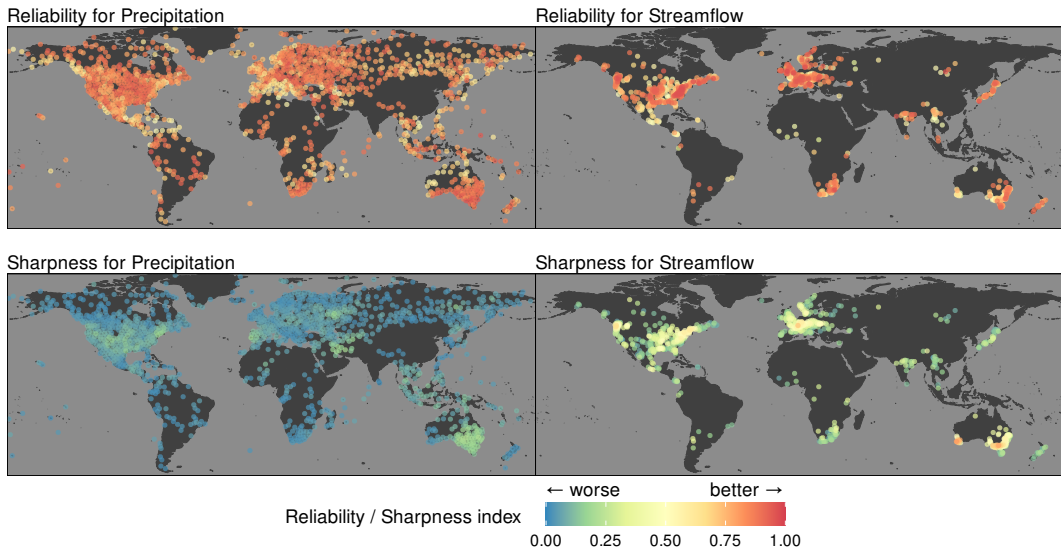


**Figure 11.** Reliability and sharpness indices associated with the reconstructed time-varying distributions (as shown in Figure 10 for two sites), for all precipitation and streamflow sites (SON season).

PIT diagrams in Figure 12a indicate a good overall reliability for both  $P$  and  $Q$  and confirm that reliability remains good in validation. Figure 12b breaks down this assessment at the station scale by showing the distribution of reliability indices. Reliability is again acceptable for both  $P$  and  $Q$  (although slightly better for the former) and there is no marked reliability loss with the validation sample. It is also of interest to compute the reliability index for each year rather than for each station in order to assess whether the reconstruction quality remains stable in time. Figure 12d suggests that this is indeed the case: reliability is stable and high (mostly above 0.9) after 1960 in all cases. It is more variable before 1960 for variable  $Q$ , but this may be attributed to sampling variability: streamflow data are indeed scarce before 1960 (see Figure 1), so that reliability indices are computed on a small number of stations for earlier years. Finally, Figure 12c shows the distribution of sharpness indices across stations. It confirms that  $Q$  reconstructions are much sharper than  $P$  ones, and it also suggests a noticeable loss of sharpness for the validation sample.

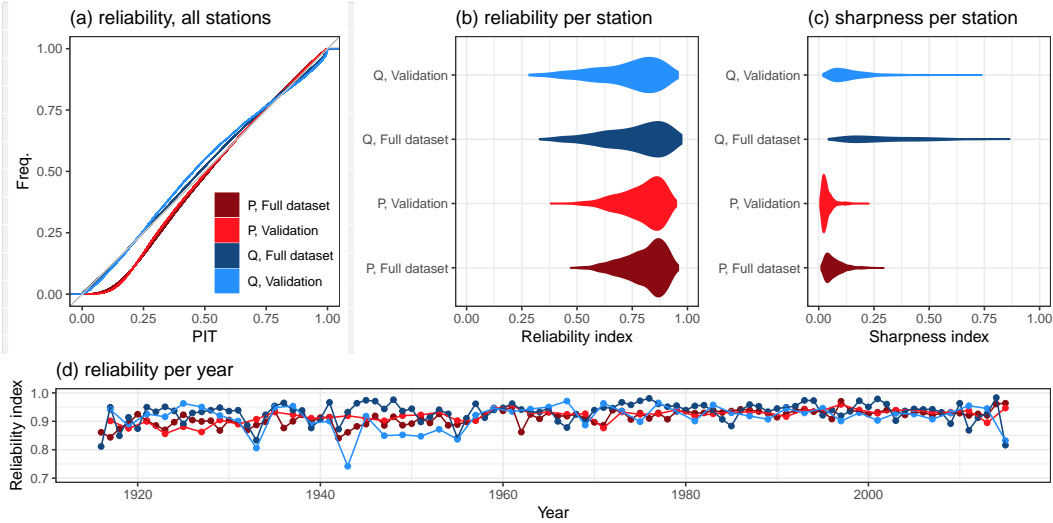


**Figure 12.** Assessment of the reliability and sharpness of reconstructed time-varying distributions in a cross-validation exercise (SON season). (a) PIT diagrams for all stations; (b) distribution of reliability indices computed by station; (c) distribution of sharpness indices computed by station; (d) time series of reliability indices computed by year.

#### 647 4.3.3 Reconstructing Probability Maps

648 A possible way to use the time-varying distributions of Section 4.3.1 is to compute  
 649 the probability of exceeding the  $T$ -year quantile at each site and in any given year. Us-  
 650 ing Figure 10 as an illustration, this corresponds to the probability of exceeding the value  
 651  $1 - 1/T$  according to the time-varying distributions. These probabilities are released as  
 652 an open dataset (see Section 7) for the four seasons and for return periods  $T = 2, 10$  and  
 653 100 years. The corresponding maps can be browsed through in the online app. Figure 13a  
 654 shows an example of such a map for the 10-year quantile (i.e.  $T = 10$ ) in SON 1903.  
 655 At each site, the probability can be compared to  $1/T = 0.1$ , which is an upper bound  
 656 for the marginal (i.e. long-term average) probability. It is only an upper bound because  
 657 the map refers to seasonal rather than annual maxima (the marginal probability would  
 658 be equal to 0.1 if annual maxima systematically fell in SON). For this particular year,  
 659 the  $P$  map does not highlight strong exceedances of the value 0.1, which is a conse-  
 660 quence of the low sharpness of  $P$ -reconstructions. At the opposite, the  $Q$  map suggests a ‘flood  
 661 hotspot’ in the Northeastern US, where the probability of a 10-year flood exceeds 0.4,  
 662 and to a lesser extent, in Northwestern US, Western Europe and Southern Australia.

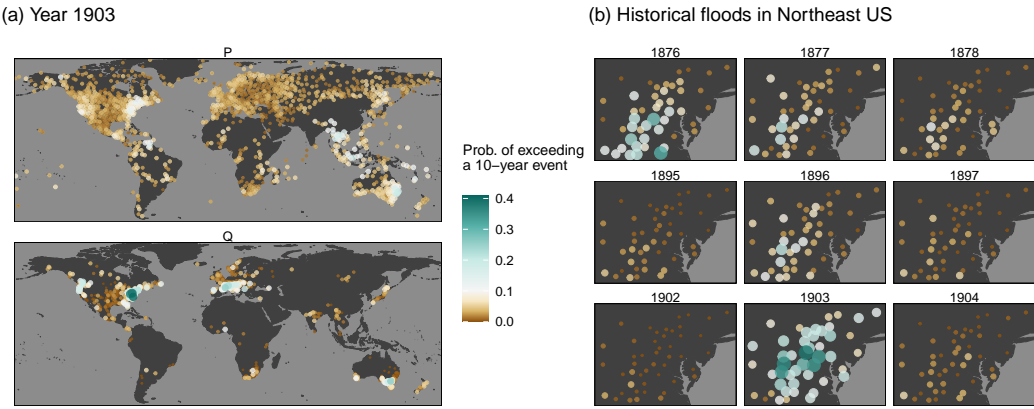


**Figure 13.** Reconstructed probabilities of exceeding a 10-year event during the SON season.

(a) Example of global maps for both heavy precipitation (top) and floods (bottom) during SON 1903. (b) Regional zoom for floods during 9 selected years. Each row shows three consecutive years, with the one in the middle column corresponding to the occurrence of a major historical flood in SON (1877, 1896 and 1903).

Figure 14 provides a synthetic view of these probability maps in SON for the whole period 1836-2015 by sorting the stations according to the AR6 region they belong to (Iturribide et al., 2020). For heavy precipitation, the most prominent feature is the clustering of higher-than-usual occurrence probabilities after  $\sim 1950$  in most regions. This indicates that atmospheric conditions have been more favorable to the occurrence of heavy precipitation events in the recent decades, in line with the widespread increase detected in station data (Section 4.1.3). Similar high-probability clusters can also be found during the 19th century in a few regions such as Eastern and Western North America (ENA and WNA). The figure for floods is quite distinct from the precipitation one: it does not highlight any widespread trend but rather region-specific patterns. In particular, high-probability clusters are visible during the mid-19th century in Western and Central Europe (WCE), in the Mediterranean (MED) and in some regions of Asia (EAS and SAS). Conversely atmospheric conditions have been less favorable to the occurrence of floods during the most recent decades in these regions. The opposite pattern is observed in Northern Europe (NEU) and in North America (WNA and ENA), with high-probability clusters appearing in recent decades.

It is also of interest to inspect in more detail specific areas, in particular those showing good reliability and sharpness (Figure 11). Here we focus on a region of the North-

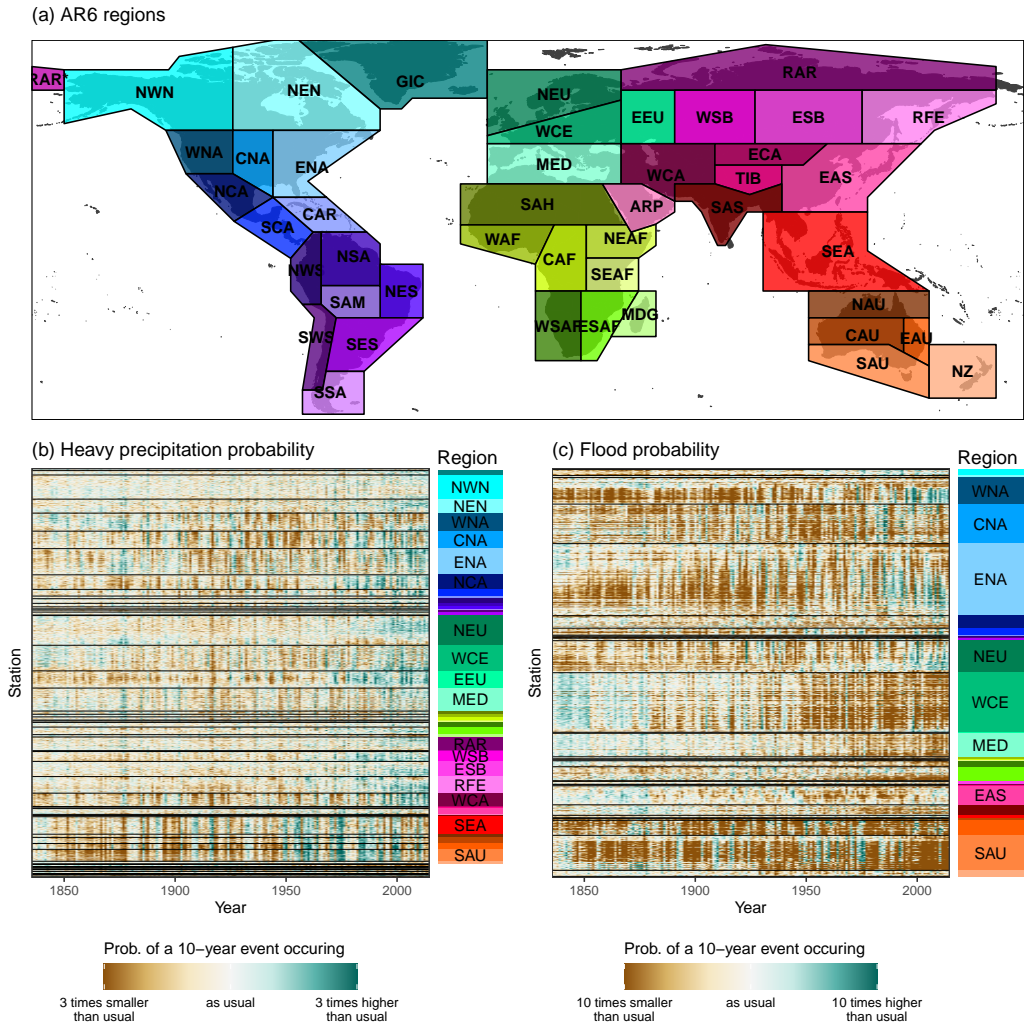


**Figure 14.** Synthetic illustration of the 180-year reconstruction for the SON season. (a) AR6 regions as defined by Iturbide et al. (2020). (b) Reconstructed probabilities of exceeding a 10-year precipitation during the SON season, for all years (columns) and stations (rows, sorted by AR6 region then by latitude within each region). Colors and acronyms in the right stripe correspond to the AR6 regions shown in panel (a). (c) Same as (b) for probabilities of exceeding a 10-year flood.

681 eastern US delimited by the Appalachian Mountains to the west, North Carolina to the  
 682 south and the State of New York to the north (Figure 13b). This region was selected due  
 683 to the availability of an inventory of historical floods provided by the NOAA-NWS Mid-  
 684 dle Atlantic River Forecast Center ([https://www.weather.gov/marfc/Flood\\_Frequency](https://www.weather.gov/marfc/Flood_Frequency)).  
 685 According to this inventory, major flooding occurred during the SON season in 1877, 1896  
 686 and 1903. Figure 13b shows the associated flood probabilities reconstructed from atmo-  
 687 spheric variables (and hence not directly using streamflow information since the  $P$  and  
 688  $Q$  datasets started in 1916). These three particular years are indeed characterized by prob-  
 689 abilities above 0.1 (middle column), and up to 4 times above it in 1903. By contrast, the  
 690 non-flood years before and after 1896 and 1903 show probabilities close to 0. The case  
 691 of 1877 is different since the previous year also shows high probabilities, but the inven-  
 692 tory does not mention any flood in 1876.

## 693 5 Discussion

### 694 5.1 How do Results from the 100-year Analysis Compare with Liter- 695 ature?

696 The joint modeling of floods and heavy precipitation and the use of a 100-period  
 697 make this study stand out from other large-scale analyses in the literature, as illustrated  
 698 in Table 1. It is therefore of interest to assess whether these specific features yield in-  
 699 sights that differ from those of the literature.

700 Overall, the results in terms of trends (or lack thereof) are remarkably consistent  
 701 with the literature. The wide-ranging trends found in P-specific HCIs are in agreement  
 702 with IPCC's statement that heavy precipitation has increased since the mid-20th cen-  
 703 tury (IPCC, 2021, chapter 11): the statement hence also holds since the early 20th cen-  
 704 tury, and it still holds for each of the four seasons (Figure 6). In contrast to heavy pre-  
 705 cipitation, trends affecting Q-specific HCIs are smaller and have much more localized ef-  
 706 fects. This is also in line with the lack of globally-consistent flood trend reported in the  
 707 literature, suggesting that this negative result is not due to the relative short period used  
 708 in most flood analyses (Table 1). Finally, trends affecting common  $P+Q$  HCIs are barely  
 709 noticeable, confirming that floods and heavy precipitation should not be expected to change  
 710 in the same way (Sharma et al., 2018), unlike annual streamflow and precipitation (Mc-  
 711 Cabe & Wolock, 2011).

712 It is also of interest to make this comparison at a smaller regional scale, for instance  
713 using the AR6 regions shown in Figure 14(a) and used in the recent analyses of Q. Sun  
714 et al. (2021, heavy precipitation) and Gudmundsson et al. (2019, floods). To achieve this,  
715 the time-varying mean of the Beta distribution ( $\mu(s, t)$  in Equation (3)) is computed for  
716 each individual station over the whole period 1916-2015. The resulting time series are  
717 grouped by AR6 region and the common regional trend is computed for each region. The  
718 corresponding figures are shown in the Supporting Information (Figures S1 to S8). For  
719 heavy precipitation (Figures S1 to S4), the trends are remarkably consistent with the  
720 results described by Q. Sun et al. (2021, in particular their Table 1). These authors re-  
721 ported mostly increasing trends in annual maxima of daily precipitation in several re-  
722 gions of North America (CNA, ENA, NCA), Europe (NEU, EEU) and Asia (WSB, RFE).  
723 For all these regions, increasing trends are also discernible over the period 1916-2015 and  
724 for most seasons (Figures S1 to S4). Conversely, regions where trends were reported as  
725 less consistent (SAU, RAR, NWN) also show no clear increasing trend in our results. The  
726 only notable discrepancy is the MED region, for which Q. Sun et al. (2021) reported rather  
727 inconsistent trends while our results show a discernible increasing trend, especially in SON  
728 which is the most extreme-prone season (Figure S1). For floods, the comparison with  
729 the results of Gudmundsson et al. (2019, in particular their Figure 3) is not as conclu-  
730 sive. One of the strongest result reported by these authors was a decrease in streamflow  
731 of the MED region, including for annual maxima, but our results highlight no clear trend  
732 in the main flood seasons (DJF and SON, Figures S6 and S5). On the other hand, the  
733 clear decreasing trend reported by Gudmundsson et al. (2019) for SAU since the 1970's  
734 is also visible for 3 seasons in our results (Figures S5 to S7), but not in JJA which is the  
735 most extreme-prone season in this region (Figures S8). Several reasons may explain this  
736 mostly inconclusive comparison for floods. First, the 100-year time period used here dif-  
737 fers from those used in the literature (see Table 1), and many authors reported that flood  
738 trends are highly sensitive to the selected period (see e.g. Hodgkins et al., 2017; Gud-  
739 mundsson et al., 2019). Moreover, we performed four separate seasonal analyses, while  
740 other comparable global-scale trend analyses worked at the annual scale, thus compli-  
741 cating direct comparisons. Finally, flood trends are overall quite weak and spatially in-  
742 consistent, making them more sensitive to data or methodological differences between  
743 studies.

Results in terms of low-frequency variability are only partly consistent with the literature. Indeed, several studies have highlighted significant clustering of flood events in time in some regions of Australia (e.g. Franks & Kuczera, 2002) or Europe (e.g. Lun et al., 2020), which should result in the presence of autocorrelation in HCIs. Some confirming evidence is found in the case of Australia: the second  $P+Q$  HCI during the MAM season has a noticeable autocorrelation (Figure 6, bottom right panel), and it mostly affects Eastern Australia. However, no noticeable autocorrelation is detected for other HCIs affecting Europe. This failure to detect flood clustering might be partly due to the lack of power of the HCI model used in this study to detect such variability. We stress, however, that the long 100-year analysis period used in this paper is beneficial in terms of detection power. Moreover, the HCI framework is not inherently unable to detect low-frequency variability, as demonstrated by Renard & Thyer (2019) using a synthetic experiment. Finally, we applied the HCI model used in this study to Sea Surface Temperature data (SST, not shown), and the model identified components with a very clear low-frequency signal. Our interpretation is therefore that low frequency variability may exist but it only accounts for a small part of the temporal variability of floods and heavy precipitation, at least when they are considered at the global scale over the last 100 years.

## 5.2 Originality of the 180-year Reconstruction

A key contribution of this work is the global reconstruction of flood and heavy precipitation probabilities since 1836. This reconstruction allows highlighting periods during which atmospheric pressure, wind and temperature conditions were favorable to the occurrence of extremes in specific regions. The widespread increase in heavy precipitation probabilities is in line with their expected behavior under a warming climate and with the increasing trends revealed by the 100-year analysis. Regarding floods, the high-probability period affecting Western, Central and Southern Europe during the mid-19th century is worth a particular note since it predates the availability of station data and is hence purely identified from atmospheric information. Interestingly, this period is consistent with one of the flood-rich period identified by Blöschl et al. (2020) using historical information. The release of the reconstruction as an open dataset makes it open to further appraisal by means of local historical data or other sources of information.

In addition to its length, the uniqueness of the reconstruction lies in the fact that it reaches a global extent while operating on station data (i.e. streamflow measured at

776 hydrometric stations and precipitation measured at raingauges). As far as we know, sim-  
 777 ilar long and station-based reconstructions have been limited to a national extent so far  
 778 (e.g. Caillouet et al., 2017; Devers et al., 2020, 2021, in France). Alternatively, global-  
 779 extent hydrologic reconstructions are generally shorter and operate on relatively large  
 780 gridcells, which makes them relevant for large catchments only. As an illustration, the  
 781 reconstruction of Alfieri et al. (2020) (1980-2018) was calibrated on catchments larger  
 782 than  $5,000 \text{ km}^2$ , which only represents around 10% of the catchments we used in this  
 783 work. The 180-year reconstruction therefore fills a gap in the landscape of hydrologic re-  
 784 constructions. A drawback of this uniqueness is that a detailed quantitative compari-  
 785 son with existing products is difficult.

786 From a methodological standpoint, this reconstruction also constitutes a proof of  
 787 concept for a ‘bottom-up’ approach that starts from hydrologic data observed on oper-  
 788 ational station networks and attempts to uncover sources of predictability from the larger-  
 789 scale climate (Figure 2). This approach is generic and could be applied to other surface  
 790 variables and other spatial or temporal scales. The ‘bottom-up’ approach is to be com-  
 791 pared with the more standard ‘top-down’ method that transforms climate inputs into  
 792 streamflow by means of hydrologic modeling (see Prudhomme et al., 2010, for a simi-  
 793 lar discussion in the context of future projections).

### 794 **5.3 Improving Reconstructions using Historical Information**

795 In this study historical information is used to identify the dates of remarkable flood  
 796 events that could be compared against reconstructed flood probabilities. While this is  
 797 the most straightforward use of this information, it does not fully take advantage of its  
 798 richness to better understand flood risk (Brázil et al., 2006). In particular, historical  
 799 information goes back in time much further than reanalyses. As a few examples, the flood  
 800 inventory used in Section 4.3.3 goes back to 1687; historical floods of large European rivers  
 801 such as the Rhône (Pichard et al., 2017) or the Rhine (Wetter et al., 2011) have been  
 802 documented since around 1300; the European historical dataset collated by Blöschl et  
 803 al. (2020) goes back 500 years; paleofloods even allow considering millennial time scales  
 804 (Wilhelm et al., 2022). In addition, regional historical datasets provide information on  
 805 the spatial structure and extent of large-scale flood events. Finally, historical data may  
 806 include information on flood intensity, albeit a possibly qualitative one.

807 A promising research avenue would therefore be to derive reconstructions of flood  
 808 and heavy precipitation probabilities based on the joint use of three sources of information:  
 809 station measurements, long atmospheric reanalyses and paleo-historical data. In  
 810 addition to the availability of large-scale, well-documented and homogeneous datasets,  
 811 a necessary ingredient to achieve this is a flexible probabilistic model that can be prop-  
 812 erly adapted to the specificity of such a mixed dataset. This includes the joint use of dif-  
 813 ferent types of data (qualitative, quantitative both discrete and continuous), the han-  
 814 dling of missing and censored values, the ability to account for the complex space-and-  
 815 time-varying availability of historical sources, etc. The HCI framework used in this study  
 816 has been built with such a flexibility as a core objective, and could hence be adapted to  
 817 perform this analysis. This has the potential to improve both the quality and the tem-  
 818 poral extent of long-term reconstructions of floods and heavy precipitation.

#### 819 **5.4 Further Improving Historical Reconstructions**

820 Several promising directions exist to improve the sharpness of probabilistic recon-  
 821 structions, globally for heavy precipitation and at least in some regions for floods. A first  
 822 direction would be to consider alternative predictor variables. For instance, atmospheric  
 823 variables such as vertical temperature gradient or vertical wind shear may be important  
 824 for extreme-generating phenomena such as hurricanes and medicanes (Cavicchia et al.,  
 825 2014). Alternatively, surface variables describing antecedent moisture and snowmelt may  
 826 also be of interest for floods (Blöschl, Hall, et al., 2019).

827 A second direction would be to avoid the seasonal averaging of atmospheric pre-  
 828 dictors. Indeed, this averaging is likely to ‘smooth out’ features that are important for  
 829 floods in small catchments and for local precipitation. The use of seasonal quantiles rather  
 830 than averages may be considered. An alternative solution would be to preserve the daily  
 831 resolution of atmospheric fields and to look for specific dynamic patterns that are asso-  
 832 ciated with floods and heavy precipitation, using for instance a lag-embedding approach  
 833 (Giannakis & Majda, 2012).

834 Finally, a third direction to improve historical reconstructions would be to lever-  
 835 age recent progress in Machine Learning (ML), in particular in neural network approaches  
 836 tailored to large spatiotemporal datasets (e.g. Nielsen et al., 2022). We note that the meth-  
 837 ods used in this work already share many similarities with ML approaches. For exam-

ple, the HCI model can be viewed as an extension of probabilistic principal component analysis (Renard et al., 2021). The prediction method described in Section 3.4 is known in ML as the inverse regression approach (see Devijver & Perthame, 2020, and reference therein for details). The idea of using HCI time series as intermediate variables when both predictor and predictand variables are highly dimensional (thousands of gridpoints/sites) is similar to the encoder-decoder approach used in ML (Murphy, 2012).

All these avenues for improvement notwithstanding, we note that there may also be intrinsic predictability limits related to the nature of floods and heavy precipitation: their high variability in both space and time make them much more difficult to predict from large-scale climate than e.g. seasonally-averaged precipitation/streamflow or smoother variables such as temperatures. As an illustration, applying the exact same framework as in this study to SST predictand yielded much sharper reconstructions than those obtained with floods and heavy precipitation (not shown).

## 5.5 The Importance of Global Station-Based Datasets

The use of large global-scale datasets does not allow performing a thorough analysis of data quality at every site. However, the quality checks and screening procedures implemented by data owners, dataset providers and ourselves provide confidence that data errors, while certainly not absent, are isolated. A more challenging issue is the adequacy of the selected streamflow stations to monitor climate-driven variability. Indeed, HCIs may compensate for omitted time-varying factors affecting the data, including anthropogenic influences (e.g. a catchment moving from natural to regulated). The main safeguard against this issue is our attempt at selecting ‘RHN-like’ stations in countries with no known RHN (Section 2.2). This procedure is far from infallible, so that regulated catchments likely made it into the analyzed dataset. However, we are confident that they did not strongly affect the results for two reasons. First, the majority of stations used in this study (66%) do come from a formal RHN. The second reason is methodological: the spatial model used for HCI effects (Equation (4)) favors the identification of HCIs having a smooth and consistent effect at the regional scale. Isolated stations affected by non-climatic changes are hence unlikely to be picked up by the first few HCIs, unless these changes have a wide-ranging spatial effect (e.g. a change in the measurement process affecting a whole country).

869        The challenges discussed above apply to any study trying to identify climate-driven  
 870        trends or variability in hydrologic regimes. Consequently, initiatives aimed at collating  
 871        global station-based datasets and documenting their properties are of prime importance.  
 872        As an illustration, the recent ROBIN initiative (<https://www.ceh.ac.uk/our-science/projects/robin>) is an important step toward collating existing RHNs at the global scale.  
 873        More generally, a perennial approach to collating and managing multi-national stream-  
 874        flow datasets - RHN or not - is needed to avoid recurring difficulties such as homogeniz-  
 875        ing quality flags, documenting infilling procedures, detecting duplicates, performing reg-  
 876        ular updates etc. We therefore second the call by Gudmundsson et al. (2018b) for '*the*  
 877        *hydrological community [...] to collectively improve the organization of initiatives for co-*  
 878        *ordinated systems that facilitate updating, storage and documentation of existing data,*  
 879        *and to lobby for existing closed databases to be made open and accessible*'.

## 881        6 Conclusion

882        Understanding how floods and heavy precipitation may evolve in a changing cli-  
 883        mate requires characterizing their historical space-time variability as well as their co-variability.  
 884        The overarching aim of this study was to contribute to this characterization by means  
 885        of two long and global-scale analyses. The first analysis jointly explores floods and heavy  
 886        precipitation station data over a 100-year period. The second analysis provides a 180-  
 887        year reconstruction of flood and heavy precipitation probabilities derived from atmospheric  
 888        information.

889        The 100-year analysis highlights wide-ranging increasing trends affecting heavy pre-  
 890        cipitation, whereas flood trends are weaker, may be upward or downward and affect smaller  
 891        regions. These results mostly confirm literature findings (e.g. Sharma et al., 2018; IPCC,  
 892        2021) and put them on firmer ground by extending the analysis period (100-year vs. the  
 893        typical 50-to-60-year used in the literature) and jointly analyzing floods and heavy pre-  
 894        cipitation. Despite its length, the analysis does not detect strong persistence components  
 895        affecting the data, suggesting that low-frequency variability accounts for a small frac-  
 896        tion of the temporal variability of floods and heavy precipitation.

897        The second analysis provides a 180-year, global-scale reconstruction of flood and  
 898        heavy precipitation probabilities, based on atmospheric pressure, wind and temperature  
 899        variables taken from the 20CRv3 reanalysis. This reconstruction was found to be reli-

able for both floods and heavy precipitation, but sharpness is much higher for the former than for the latter. In general, higher-than-usual precipitation probabilities were found to cluster in the latest decades, reflecting atmospheric conditions favorable to the occurrence of heavy precipitation events, as expected under a warming climate (IPCC, 2021). Flood probabilities patterns did not follow such a general behavior and were found to be much more region- and season-specific. The reconstruction allowed identifying regions with abnormally high flood probabilities in the distant past, for years well before the establishment of perennial station networks. The reconstruction is released as an open dataset, which may enable more in-depth analyses at smaller spatial scales, using local historical datasets or other sources of information.

From a methodological standpoint, the HCI approach used in this study has several decisive advantages for analyzing station-based datasets. It naturally accommodates varying data availability: this avoids restricting the analysis to either a short period common to many stations or a long period for a few stations. The approach also allows analyzing the covariability of several variables measured on distinct networks by assuming that they are under the influence of common HCIs. Finally, it simplifies the derivation of relationships between highly dimensional predictor and predictand variables by using the HCI time series as low-dimensional intermediate variables. The HCI approach is very general and could hence be applied to study the historical variability of other phenomena at a large spatial scale. This includes other aspects of the hydrologic regime such as water resources and droughts, but also other variables characterizing the state of ecosystems in the context of a changing climate.

Station datasets originating from long-term monitoring networks constitute a most valuable asset to understand the historical variability of hydro-climatic variables. The statistical models used to analyze these datasets should be flexible enough to adapt to their peculiarities and make the best possible use of available data. This may improve not only the characterization of natural variability, but also the ability to derive predictive methods for past reconstructions or future projections.

## 7 Acknowledgments

This project has received funding from the European Union’s Horizon 2020 research and innovation program under the Marie Skłodowska-Curie grant agreement No 835496.

931 This work was supported with supercomputing resources provided by the Phoenix HPC  
 932 service at the University of Adelaide and the HIICS cluster at INRAE.

933 Support for the Twentieth Century Reanalysis Project dataset is provided by the  
 934 U.S. Department of Energy, Office of Science Biological and Environmental Research (BER)  
 935 program, by the National Oceanic and Atmospheric Administration Climate Program  
 936 Office, and by the NOAA Physical Sciences Laboratory.

937 Robert Dunn, Nicholas Herold, Hong Xuan Do and Lukas Gudmundsson are grate-  
 938 fully acknowledged for their insights on HadEX and GSIM datasets. We also thank the  
 939 Editor and three anonymous Reviewers for their insightful comments.

## 940 Open Research

941 All data used in this article originate from open datasets, as cited in the text. The  
 942 following repositories have been created to complement the article:

- 943 • The 180-year reconstruction and the station data for streamflow and precipita-  
 944 tion seasonal maxima are available in a Zenodo repository (Renard, 2023b, <https://doi.org/10.5281/zenodo.7680097>)
- 945 • R scripts used for setting up models, analysing results, preparing figures and the  
 946 interactive app are available in a Zenodo repository (Renard, 2023a, <https://doi.org/10.5281/zenodo.7680594>)
- 947 • MCMC simulations have been performed with the following computing codes:  
 948   – STooDs v0.1.0 (Renard, 2021b, <https://github.com/STooDs-tools/STooDs>)  
 949   – R interface RSTooDs v0.1.1 (Renard, 2021a, <https://github.com/STooDs-tools/RSTooDs>)

952 The interactive app to browse through the results for all seasons and variables is  
 953 also available online at <https://hydroapps.recover.inrae.fr/HEGS-paper>

## 954 References

- 955 Alfieri, L., Lorini, V., Hirpa, F. A., Harrigan, S., Zsoter, E., Prudhomme, C., &  
 956 Salamon, P. (2020). A global streamflow reanalysis for 1980–2018. *Journal of  
     Hydrology X*. doi: 10.1016/j.hydroa.2019.100049
- 957 Aryal, S. K., Bates, B. C., Campbell, E. P., Li, Y., Palmer, M. J., & Viney, N. R.  
 958 (2009). Characterizing and modeling temporal and spatial trends in rainfall ex-

- 960 tremes. *Journal of Hydrometeorology*, 10(1). doi: 10.1175/2008JHM1007.1
- 961 Banerjee, S. (2017). High-dimensional bayesian geostatistics. *Bayesian Anal.*, 12(2).  
962 doi: 10.1214/17-BA1056R
- 963 Berghuijs, W. R., Aalbers, E. E., Larsen, J. R., Trancoso, R., & Woods, R. A.  
964 (2017). Recent changes in extreme floods across multiple continents. *Environmental  
965 Research Letters*, 12(11). doi: 10.1088/1748-9326/aa8847
- 966 Bertola, M., Viglione, A., Lun, D., Hall, J., & Blöschl, G. (2020). Flood trends in  
967 europe: are changes in small and big floods different? *Hydrology and Earth System  
968 Sciences*, 24(4). doi: 10.5194/hess-24-1805-2020
- 969 Bertola, M., Viglione, A., Vorogushyn, S., Lun, D., Merz, B., & Blöschl, G. (2021).  
970 Do small and large floods have the same drivers of change? a regional attribu-  
971 tion analysis in europe. *Hydrology and Earth System Sciences*, 25(3). doi:  
972 10.5194/hess-25-1347-2021
- 973 Blöschl, G., Bierkens, M. F. P., Chambel, A., Cudennec, C., Destouni, G., Fiori,  
974 A., ... Zhang, Y. (2019). Twenty-three unsolved problems in hydrology  
975 (UPH) – a community perspective. *Hydrological Sciences Journal*. doi:  
976 10.1080/02626667.2019.1620507
- 977 Blöschl, G., Hall, J., Parajka, J., Perdigão, R. A. P., Merz, B., Arheimer, B., ...  
978 Živković, N. (2017). Changing climate shifts timing of european floods. *Science*,  
979 357(6351). doi: 10.1126/science.aan2506
- 980 Blöschl, G., Hall, J., Viglione, A., Perdigão, R. A. P., Parajka, J., Merz, B., ...  
981 Živković, N. (2019). Changing climate both increases and decreases european river  
982 floods. *Nature*, 573(7772). doi: 10.1038/s41586-019-1495-6
- 983 Blöschl, G., Kiss, A., Viglione, A., Barriendos, M., Böhm, O., Brázdil, R., ... Wet-  
984 ter, O. (2020). Current european flood-rich period exceptional compared with past  
985 500 years. *Nature*, 583(7817). doi: 10.1038/s41586-020-2478-3
- 986 Bonnet, R., Boé, J., Dayon, G., & Martin, E. (2017). Twentieth-century hydrome-  
987 teorological reconstructions to study the multidecadal variations of the water cycle  
988 over france. *Water Resources Research*, 53(10). doi: 10.1002/2017WR020596
- 989 Brunner, M. I., Swain, D. L., Wood, R. R., Willkofer, F., Done, J. M., Gilleland, E.,  
990 & Ludwig, R. (2021). An extremeness threshold determines the regional response  
991 of floods to changes in rainfall extremes. *Communications Earth & Environment*.  
992 doi: 10.1038/s43247-021-00248-x

- 993 Brázdil, R., Kundzewicz, Z. W., & Benito, G. (2006). Historical hydrology for study-  
994 ing flood risk in europe. *Hydrological Sciences Journal*, 51, 739–764. doi: 10.1623/  
995 hysj.51.5.739
- 996 Bureau of Meteorology. (2020). *Hydrologic reference stations - update 2020*. Re-  
997 trieved from [http://www.bom.gov.au/water/hrs/update\\_2020.shtml](http://www.bom.gov.au/water/hrs/update_2020.shtml)
- 998 Burn, D. H., Hannaford, J., Hodgkins, G. A., Whitfield, P. H., Thorne, R., &  
999 Marsh, T. (2012). Reference hydrologic networks II. using reference hydrologic  
1000 networks to assess climate-driven changes in streamflow. *Hydrological Sciences  
1001 Journal*. doi: 10.1080/02626667.2012.728705
- 1002 Burn, D. H., & Whitfield, P. H. (2017). Changes in cold region flood regimes in-  
1003 ferred from long-record reference gauging stations. *Water Resources Research*,  
1004 53(4). doi: 10.1002/2016WR020108
- 1005 Burn, D. H., & Whitfield, P. H. (2018). Changes in flood events inferred from cen-  
1006 tennial length streamflow data records. *Advances in Water Resources*, 121. doi:  
1007 10.1016/j.advwatres.2018.08.017
- 1008 Caillouet, L., Vidal, J. P., Sauquet, E., Devers, A., & Graff, B. (2017). Ensemble re-  
1009 construction of spatio-temporal extreme low-flow events in france since 1871. *Hy-  
1010 drology and Earth System Sciences*, 21(6). doi: 10.5194/hess-21-2923-2017
- 1011 Caillouet, L., Vidal, J.-P., Sauquet, E., Devers, A., Lauvernet, C., Graff, B., & Van-  
1012 nier, O. (2021). Intercomparaison des évènements d'étiage extrême en france  
1013 depuis 1871. *LHB*, 107(1). doi: 10.1080/00186368.2021.1914463
- 1014 Caillouet, L., Vidal, J. P., Sauquet, E., & Graff, B. (2016). Probabilistic precipita-  
1015 tion and temperature downscaling of the twentieth century reanalysis over france.  
1016 *Climate of the Past*, 12(3). doi: 10.5194/cp-12-635-2016
- 1017 Cavicchia, L., von Storch, H., & Gualdi, S. (2014). A long-term climatology of medi-  
1018 canes. *Climate Dynamics*, 43(5). doi: 10.1007/s00382-013-1893-7
- 1019 Compo, G. P., Whitaker, J. S., Sardeshmukh, P. D., Matsui, N., Allan, R. J., Yin,  
1020 X., ... Worley, S. J. (2011). The twentieth century reanalysis project. *Quarterly  
1021 Journal of the Royal Meteorological Society*, 137(654). doi: 10.1002/qj.776
- 1022 Datta, A., Banerjee, S., Finley, A. O., & Gelfand, A. E. (2016a). Hierarchi-  
1023 cal nearest-neighbor gaussian process models for large geostatistical datasets.  
1024 *Journal of the American Statistical Association*, 111(514). doi: 10.1080/  
1025 01621459.2015.1044091

- 1026 Datta, A., Banerjee, S., Finley, A. O., & Gelfand, A. E. (2016b). On nearest-  
 1027 neighbor gaussian process models for massive spatial data. *Wiley Interdisciplinary*  
 1028 *Reviews: Computational Statistics*, 8(5), 162–171. doi: 10.1002/wics.1383
- 1029 Devers, A., Vidal, J., Lauvernet, C., Graff, B., & Vannier, O. (2020). A framework  
 1030 for high-resolution meteorological surface reanalysis through offline data assimila-  
 1031 tion in an ensemble of downscaled reconstructions. *Quarterly Journal of the Royal*  
 1032 *Meteorological Society*, 146(726), 153–173. doi: 10.1002/qj.3663
- 1033 Devers, A., Vidal, J.-P., Lauvernet, C., & Vannier, O. (2021). FYRE Climate: a  
 1034 high-resolution reanalysis of daily precipitation and temperature in France from  
 1035 1871 to 2012. *Climate of the Past*. doi: 10.5194/cp-17-1857-2021
- 1036 Devijver, E., & Perthame, E. (2020). Prediction regions through inverse regres-  
 1037 sion. *Journal of Machine Learning Research*, 21(113). Retrieved from <http://jmlr.org/papers/v21/19-535.html>
- 1039 Do, H. X., Gudmundsson, L., Leonard, M., & Westra, S. (2018). The global  
 1040 streamflow indices and metadata archive (GSIM) – part 1: The production of  
 1041 a daily streamflow archive and metadata. *Earth Syst. Sci. Data*, 10(2). doi:  
 1042 10.5194/essd-10-765-2018
- 1043 Do, H. X., Westra, S., & Leonard, M. (2017). A global-scale investigation of trends  
 1044 in annual maximum streamflow. *Journal of Hydrology*, 552. doi: <https://doi.org/10.1016/j.jhydrol.2017.06.015>
- 1046 Do, H. X., Zhao, F., Westra, S., Leonard, M., Gudmundsson, L., Boulange, J. E. S.,  
 1047 ... Wada, Y. (2020). Historical and future changes in global flood magnitude –  
 1048 evidence from a model–observation investigation. *Hydrology and Earth System*  
 1049 *Sciences*, 24(3). doi: 10.5194/hess-24-1543-2020
- 1050 Donat, M. G., Alexander, L. V., Yang, H., Durre, I., Vose, R., Dunn, R. J. H., ...  
 1051 Kitching, S. (2013). Updated analyses of temperature and precipitation extreme  
 1052 indices since the beginning of the twentieth century: The HadEX2 dataset. *Jour-*  
 1053 *nal of Geophysical Research: Atmospheres*, 118(5). doi: 10.1002/jgrd.50150
- 1054 Dudley, R. W., Hodgkins, G. A., McHale, M. R., Kolian, M. J., & Renard, B.  
 1055 (2017). Trends in snowmelt-related streamflow timing in the conterminous  
 1056 united states. *Journal of Hydrology*, 547. doi: <http://dx.doi.org/10.1016/j.jhydrol.2017.01.051>
- 1058 Dunn, R. J. H., Alexander, L. V., Donat, M. G., Zhang, X., Bador, M., Herold, N.,

- 1059 ... Bin Hj Yussof, M. N. (2020). Development of an updated global land in situ-based data set of temperature and precipitation extremes: HadEX3. *Journal of  
1060 Geophysical Research: Atmospheres*, 125(16). doi: 10.1029/2019JD032263
- 1061  
1062 Franks, S. W., & Kuczera, G. (2002). Flood frequency analysis: Evidence and impli-  
1063 cations of secular climate variability, new south wales. *Water Resources Research*,  
1064 38(5). doi: 10.1029/2001WR000232
- 1065 Gelman, A., & Rubin, D. B. (1992). Inference from iterative simulation using multi-  
1066 ple sequences. *Statistical Science*, 7(4). doi: 10.2307/2246093
- 1067 Giannakis, D., & Majda, A. J. (2012). Nonlinear laplacian spectral analysis for  
1068 time series with intermittency and low-frequency variability. *Proceedings of the  
1069 National Academy of Sciences of the United States of America*, 109(7). doi:  
1070 DOI10.1073/pnas.1118984109
- 1071 Global Runoff Data Centre. (2015). *Twelfth Meeting of the GRDC Steering Com-  
1072 mittee: 18-19 June 2015, Koblenz, Germany* (Tech. Rep.). Bundesanstalt für  
1073 Gewässerkunde, Koblenz. Retrieved 2023-01-20, from [http://doi.bafg.de/BfG/2015/GRDC\\_Report\\_46.pdf](http://doi.bafg.de/BfG/2015/GRDC_Report_46.pdf) doi: 10.5675/GRDC\_REPORT\_46
- 1074  
1075 Gudmundsson, L., Do, H. X., Leonard, M., & Westra, S. (2018a). *The global  
1076 streamflow indices and metadata archive (GSIM) - part 2: Time series indices and  
1077 homogeneity assessment*. PANGAEA - Data Publisher for Earth & Environmental  
1078 Science. Retrieved from <https://doi.pangaea.de/10.1594/PANGAEA.887470>
- 1079 Gudmundsson, L., Do, H. X., Leonard, M., & Westra, S. (2018b). The global  
1080 streamflow indices and metadata archive (GSIM) – part 2: Quality control, time-  
1081 series indices and homogeneity assessment. *Earth Syst. Sci. Data*, 10(2). doi:  
1082 10.5194/essd-10-787-2018
- 1083 Gudmundsson, L., Leonard, M., Do, H. X., Westra, S., & Seneviratne, S. I. (2019).  
1084 Observed trends in global indicators of mean and extreme streamflow. *Geophysical  
1085 Research Letters*, 46(2). doi: 10.1029/2018GL079725
- 1086 Hall, J., Arheimer, B., Borga, M., Brázil, R., Claps, P., Kiss, A., ... Blöschl,  
1087 G. (2014). Understanding flood regime changes in europe: a state-of-the-  
1088 art assessment. *Hydrology and Earth System Sciences*, 18(7). doi: 10.5194/  
1089 hess-18-2735-2014
- 1090 Hannachi, A., Jolliffe, I. T., & Stephenson, D. B. (2007). Empirical orthogonal func-  
1091 tions and related techniques in atmospheric science: A review. *International Jour-*

- 1092         nal of Climatology, 27(9). doi: 10.1002/joc.1499
- 1093         Henley, B. J., Thyer, M. A., Kuczera, G., & Franks, S. W. (2011). Climate-informed  
1094         stochastic hydrological modeling: Incorporating decadal-scale variability using  
1095         paleo data. *Water Resources Research*. doi: 10.1029/2010WR010034
- 1096         Hodgkins, G. A., Whitfield, P. H., Burn, D. H., Hannaford, J., Renard, B., Stahl,  
1097         K., ... Wilson, D. (2017). Climate-driven variability in the occurrence of ma-  
1098         jor floods across north america and europe. *Journal of Hydrology*, 552. doi:  
1099         <https://doi.org/10.1016/j.jhydrol.2017.07.027>
- 1100         IPCC. (2021). *Climate change 2021: The physical science basis. contribution of  
1101         working group I to the sixth assessment report of the intergovernmental panel on  
1102         climate change.*
- 1103         Iturbide, M., Gutiérrez, J. M., Alves, L. M., Bedia, J., Cerezo-Mota, R., Cimadev-  
1104         illa, E., ... Vera, C. S. (2020). An update of IPCC climate reference regions for  
1105         subcontinental analysis of climate model data: definition and aggregated datasets.  
1106         *Earth System Science Data*. doi: 10.5194/essd-12-2959-2020
- 1107         Laio, F., & Tamea, S. (2007). Verification tools for probabilistic forecasts of continu-  
1108         ous hydrological variables. *Hydrology and Earth System Sciences*, 11(4).
- 1109         Lee, D., Ward, P., & Block, P. (2018). Attribution of Large-Scale Climate Patterns  
1110         to Seasonal Peak-Flow and Prospects for Prediction Globally. *Water Resources  
1111         Research*. doi: 10.1002/2017WR021205
- 1112         Liu, J., & Zhang, Y. (2017). Multi-temporal clustering of continental floods and  
1113         associated atmospheric circulations. *Journal of Hydrology*, 555. doi: 10.1016/j  
1114         .jhydrol.2017.10.072
- 1115         Lun, D., Fischer, S., Viglione, A., & Blöschl, G. (2020). Detecting flood-rich and  
1116         flood-poor periods in annual peak discharges across europe. *Water Resources Re-  
1117         search*, 56(7). doi: 10.1029/2019WR026575
- 1118         McCabe, G. J., & Wolock, D. M. (2011). Independent effects of temperature and  
1119         precipitation on modeled runoff in the conterminous United States: EFFECTS  
1120         OF TEMPERATURE AND PRECIPITATION ON RUNOFF. *Water Resources  
1121         Research*. doi: 10.1029/2011WR010630
- 1122         Mediero, L., Kjeldsen, T., Macdonald, N., Kohnova, S., Merz, B., Vorogushyn, S.,  
1123         ... Porarinsson, O. (2015). Identification of coherent flood regions across eu-  
1124         rope by using the longest streamflow records. *Journal of Hydrology*, 528. doi:

- 1125 10.1016/j.jhydrol.2015.06.016
- 1126 Merz, B., Nguyen, V. D., & Vorogushyn, S. (2016). Temporal clustering of floods in  
1127 germany: Do flood-rich and flood-poor periods exist? *Journal of Hydrology*, 541.  
1128 doi: <https://doi.org/10.1016/j.jhydrol.2016.07.041>
- 1129 Murphy, K. P. (2012). *Machine learning: a probabilistic perspective*. MIT Press.
- 1130 Najibi, N., & Devineni, N. (2018). Recent trends in the frequency and duration of  
1131 global floods. *Earth System Dynamics*. doi: 10.5194/esd-9-757-2018
- 1132 Nielsen, A. H., Iosifidis, A., & Karstoft, H. (2022). Forecasting large-scale circulation  
1133 regimes using deformable convolutional neural networks and global spatiotemporal  
1134 climate data. *Scientific Reports*, 12. doi: 10.1038/s41598-022-12167-8
- 1135 Papalexiou, S. M., & Montanari, A. (2019). Global and regional increase of precipi-  
1136 tation extremes under global warming. *Water Resources Research*, 55(6). doi: 10  
1137 .1029/2018wr024067
- 1138 Pichard, G., Arnaud-Fassetta, G., Moron, V., & Roucaute, E. (2017). Hydro-  
1139 climatology of the lower rhône valley: historical flood reconstruction (AD  
1140 1300–2000) based on documentary and instrumental sources. *Hydrological Sci-  
1141 ences Journal*, 62(11). doi: 10.1080/02626667.2017.1349314
- 1142 Poli, P., Hersbach, H., Dee, D. P., Berrisford, P., Simmons, A. J., Vitart, F., ...  
1143 Fisher, M. (2016). ERA-20C: An Atmospheric Reanalysis of the Twentieth  
1144 Century. *Journal of Climate*, 29(11). doi: doi:10.1175/JCLI-D-15-0556.1
- 1145 Prudhomme, C., Wilby, R., Crooks, S., Kay, A., & Reynard, N. (2010). Scenario-  
1146 neutral approach to climate change impact studies: Application to flood risk.  
1147 *Journal of Hydrology*. doi: 10.1016/j.jhydrol.2010.06.043
- 1148 Radanovics, S., Vidal, J. P., Sauquet, E., Ben Daoud, A., & Bontron, G. (2013). Op-  
1149 timising predictor domains for spatially coherent precipitation downscaling. *Hy-  
1150 drology and Earth System Sciences*, 17(10). doi: 10.5194/hess-17-4189-2013
- 1151 Renard, B. (2021a). *STooDs-tools/RSTooDs: RSTooDs package v0.1.1 [soft-  
1152 ware]*. Retrieved from <https://zenodo.org/record/5075760> doi: 10.5281/  
1153 zenodo.5075760
- 1154 Renard, B. (2021b). *STooDs-tools/STooDs: STooDs engine v0.1.0 [soft-  
1155 ware]*. Retrieved from <https://zenodo.org/record/5075586> doi: 10.5281/  
1156 ZENODO.5075586
- 1157 Renard, B. (2023a). *Codes and data related to the article: 'Renard et al. Floods*

- 1158 and Heavy Precipitation at the Global Scale: 100-year Analysis and 180-year Re-  
1159 construction. *Journal of Geophysical Research - Atmospheres* (version 1.0.0)  
1160 [software]. Zenodo. Retrieved from <https://zenodo.org/record/7680594> doi:  
1161 10.5281/ZENODO.7680594
- 1162 Renard, B. (2023b). Global reconstruction of flood and heavy precipitation probabili-  
1163 ties, 1836-2015 (version 1.1.0) [dataset]. Zenodo. Retrieved from <https://zenodo.org/record/7680097> doi: 10.5281/ZENODO.7680097
- 1164 Renard, B., Garreta, V., & Lang, M. (2006). An application of bayesian analysis and  
1165 markov chain monte carlo methods to the estimation of a regional trend in annual  
1166 maxima. *Water Resources Research*, 42(12). doi: 10.1029/2005WR004591
- 1167 Renard, B., Kavetski, D., Thyer, M., Kuczera, G., & Franks, S. W. (2010). Under-  
1168 standing predictive uncertainty in hydrologic modeling: The challenge of identify-  
1169 ing input and structural errors. *Water Resources Research*, 46.
- 1170 Renard, B., Lang, M., Bois, P., Dupeyrat, A., Mestre, O., Niel, H., ... Gail-  
1171 hard, J. (2008). Regional methods for trend detection: Assessing field sig-  
1172 nificance and regional consistency. *Water Resources Research*, 44(8). doi:  
1173 10.1029/2007WR006268
- 1174 Renard, B., & Thyer, M. (2019). Revealing hidden climate indices from the oc-  
1175 currence of hydrologic extremes. *Water Resources Research*. doi: 10.1029/  
1176 2019WR024951
- 1177 Renard, B., Thyer, M., McInerney, D., Kavetski, D., Leonard, M., & Westra, S.  
1178 (2021). A hidden climate indices modeling framework for multi-variable space-  
1179 time data. *Water Resources Research*. doi: 10.1029/2021WR030007
- 1180 Sharma, A., Wasko, C., & Lettenmaier, D. P. (2018). If precipitation extremes are  
1181 increasing, why aren't floods? *Water Resources Research*, 54(11). doi: 10.1029/  
1182 2018wr023749
- 1183 Slater, L., Villarini, G., Archfield, S., Faulkner, D., Lamb, R., Khouakhi, A., & Yin,  
1184 J. (2021). Global Changes in 20-Year, 50-Year, and 100-Year River Floods.  
1185 *Geophysical Research Letters*. doi: 10.1029/2020GL091824
- 1186 Slater, L. J., Anderson, B., Buechel, M., Dadson, S., Han, S., Harrigan, S., ...  
1187 Wilby, R. L. (2020). Nonstationary weather and water extremes: a review of  
1188 methods for their detection, attribution, and management. *Hydrology and Earth  
1189 System Sciences*. doi: 10.5194/hess-2020-576

- Slivinski, L. C., Compo, G. P., Whitaker, J. S., Sardeshmukh, P. D., Giese, B. S.,  
McColl, C., ... Wyszyński, P. (2019). Towards a more reliable historical reanalysis: Improvements for version 3 of the twentieth century reanalysis system. *Quarterly Journal of the Royal Meteorological Society*, 145(724). doi: 10.1002/qj.3598
- Stahl, K., Tallaksen, L. M., Hannaford, J., & van Lanen, H. A. J. (2012). Filling the white space on maps of european runoff trends: estimates from a multi-model ensemble. *Hydrology and Earth System Sciences*, 16(7). doi: 10.5194/hess-16-2035-2012
- Sun, Q., Zhang, X., Zwiers, F., Westra, S., & Alexander, L. V. (2021). A global, continental, and regional analysis of changes in extreme precipitation. *Journal of Climate*, 34(1). doi: 10.1175/JCLI-D-19-0892.1
- Sun, X., & Lall, U. (2015). Spatially coherent trends of annual maximum daily precipitation in the united states. *Geophysical Research Letters*, 42(22). doi: doi:10.1002/2015GL066483
- Sun, X., Renard, B., Thyer, M., Westra, S., & Lang, M. (2015). A global analysis of the asymmetric effect of ENSO on extreme precipitation. *Journal of Hydrology*. doi: <http://dx.doi.org/10.1016/j.jhydrol.2015.09.016>
- Tipping, M. E., & Bishop, C. M. (1999). Probabilistic Principal Component Analysis. *Journal of the Royal Statistical Society: Series B (Statistical Methodology)*. doi: 10.1111/1467-9868.00196
- Tramblay, Y., Mimeau, L., Neppel, L., Vinet, F., & Sauquet, E. (2019). Detection and attribution of flood trends in mediterranean basins. *Hydrology and Earth System Sciences*, 23(11). doi: 10.5194/hess-23-4419-2019
- Wei, W., Yan, Z., & Li, Z. (2021). Influence of pacific decadal oscillation on global precipitation extremes. *Environmental Research Letters*, 16(4). doi: 10.1088/1748-9326/abed7c
- Westra, S., Alexander, L. V., & Zwiers, F. W. (2012). Global increasing trends in annual maximum daily precipitation. *Journal of Climate*. doi: 10.1175/jcli-d-12-00502.1
- Wetter, O., Pfister, C., Weingartner, R., Luterbacher, J., Reist, T., & Trösch, J. (2011). The largest floods in the high rhine basin since 1268 assessed from documentary and instrumental evidence. *Hydrological Sciences Journal*, 56. doi: 10.1080/02626667.2011.583613

- 1224 Whitfield, P. H., Burn, D. H., Hannaford, J., Higgins, H., Hodgkins, G. A., Marsh,  
1225 T., & Looser, U. (2012). Reference hydrologic networks i. the status and potential  
1226 future directions of national reference hydrologic networks for detecting trends.  
1227 *Hydrological Sciences Journal*. doi: 10.1080/02626667.2012.728706
- 1228 Wilhelm, B., Rapuc, W., Amann, B., Anselmetti, F. S., Arnaud, F., Blanchet, J.,  
1229 ... Wirth, S. B. (2022). Impact of warmer climate periods on flood hazard in the  
1230 european alps. *Nature Geoscience*, 15(2). doi: 10.1038/s41561-021-00878-y